nature communications

Article

https://doi.org/10.1038/s41467-025-59607-3

Dynamics of a light-driven molecular rotary motor in an optical cavity

Received: 19 September 2024

Accepted: 28 April 2025

Published online: 16 May 2025

Check for updates

In Seong Lee[1], Michael Filatov[1] ✉ & Seung Kyu Min[1,2] ✉

Light-driven rotary molecular motors transform the energy of light to mechanical motion (rotation) of one part of the molecule with respect to another. For a long while, various stimuli orthogonal to the motor's source of energy were used to manipulate its operational characteristics; such as the speed of rotation. However, these stimuli employed predominantly chemical means and were difficult to apply in situ during the motor's operation. Here, we show that the characteristics of the excited state decay in molecular motor molecules can be altered due to strong light-matter interactions occurring in optical cavities. By performing nonadiabatic simulations of the motor's photodynamics in the presence of strong coupling with a cavity mode, we find that the coupling with a mode detuned off resonance with the molecular optical transition offers a means to considerably increase the excited state decay lifetime and to either inhibit or slow down the motor's rotation.

Light-driven rotary molecular motors[1–3] (LDRMs) can transform the energy of light to rotary motion of one part of the molecule (usually termed rotator) with respect to another (stator)[4–8]. The energy of the mechanical motion can be harnessed in various nanosized devices, which already find first applications in fields such as nanotechnology, optogenetics, synthetic biology, nanomedicine, and functional materials[8–17].

The most commonly occurring design of LDRMs involves an overcrowded alkene motif[1], where, upon photoexcitation, the energy of the steric strain of the central double bond (see Fig. 1) is released in the form of rotary motion. Typically, the working cycle of such a motor involves four distinct steps, which are shown in Fig. 1a[18]. Initially in a thermodynamically stable configuration, (M)-(S)-**1**, the motor undergoes photoisomerization to a metastable (P)-(S)-**1** configuration, where the methyl group at the stereogenic centre attains a less favorable equatorial orientation; see Fig. 1a. Upon undergoing thermally activated (P → M) helix inversion, where the rotator migrates over the stator, the motor settles in a (M)-(S)-**1** configuration with the rotator rotated through 180° with respect to its initial orientation at the beginning of the cycle. Although both stable configurations (in the upper left and lower right corners of Figure 1a) are completely equivalent, it is convenient to label them as Z (or cis) and E (or trans) configurations according to the value (≈0° or ≈180°) of the ∠(C_{9a}–C_9=$C_{1'}$–$C_{1'a}$) dihedral angle; see Figure 1b for atom numbering. From the obtained EM structure, the second half-cycle of photoisomerization and helix inversion completes the full 360° loop[19].

When designing LDRMs for specific applications, one of the most important tasks is to gain control over their photomechanical properties. Ideally, this should be an external stimulus orthogonal to the motor's source of energy (light) and easily applicable in situ. Over the years, various chemical stimuli have been employed to modify LDRMs characteristics, such as rotation speed and direction,[20–24] absorption wavelength,[20,21] activation or deactivation of the rotational motion[25–27]. However, not all the proposed stimuli can be employed on-the-fly during the motor's operation. Besides that, it was primarily the thermally activated helix inversion step that was targeted. So far, no attempts to alter the photodynamics of the power stroke of LDRMs by external stimuli have been reported. Here, we attempt to fill in that gap by studying the effect of coupling between the molecular electronic states and a longitudinal cavity mode (a standing wave inside an optical cavity) on the photodynamics of LDRMs.

When considering phenomena occurring in excited states of molecules, the molecular electronic states and light photons are usually treated as independent entities[28]. However, when the

[1]Center for Multidimensional Carbon Materials (CMCM), Institute for Basic Science (IBS), UNIST-gil 50, Ulsan 44919, Republic of Korea. [2]Department of Chemistry, Ulsan National Institute of Science and Technology (UNIST), UNIST-gil 50, Ulsan 44919, Republic of Korea. ✉e-mail: mike.filatov@gmail.com; skmin@unist.ac.kr

https://doi.org/10.1038/s41467-025-59607-3

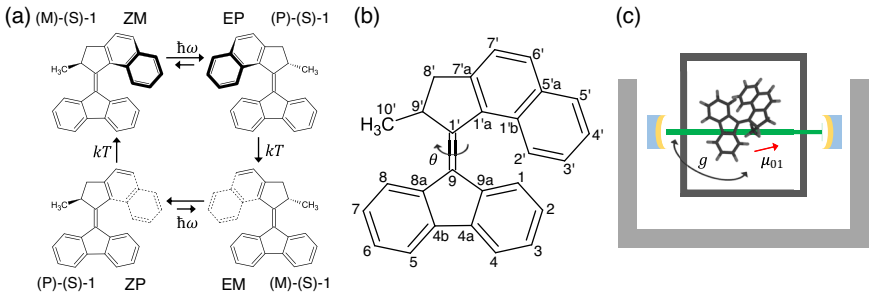

Fig. 1 | Motor-cavity system. a Schematic representation of the working mechanism of motor **1**, which results in a unidirectional rotation in the clockwise (CW) direction. The rotation begins in the stable (M)-(S)-**1** configuration, which is photochemically converted into a metastable (P)-(S)-**1** configuration ($\hbar\omega$). The thermal helix inversion step (kT) results in the stable (M)-(S)-**1** configuration, where the rotator part is rotated through 180° with respect to its orientation in the starting structure. To distinguish between the equivalent isomeric structures, a label E or Z was assigned according to the $\angle(C_{9a}{-}C_9{=}C_{1'}{-}C_{1'a})$ dihedral angle. The alternative (ZM, EP, EM, and ZP) labels are given alongside the conventional enantiomeric labels. **b** Atom numbering in fluorene motor **1**. The dihedral angle θ around the central $C_9{=}C_{1'}$ bond is defined as the angle between the (C_{8a}, C_9, C_{9a}) plane and the ($C_{9'}$, $C_{1'}$, $C_{1'a}$) plane. **c** Schematic illustration of a molecular motor coupled to a gas-phase optical cavity. The photoisomerization reaction around the central $C_9{=}C_{1'}$ bond can be controlled by the coupling strength g and the transition dipole moment $\boldsymbol{\mu}_{01}$ between the electronic states.

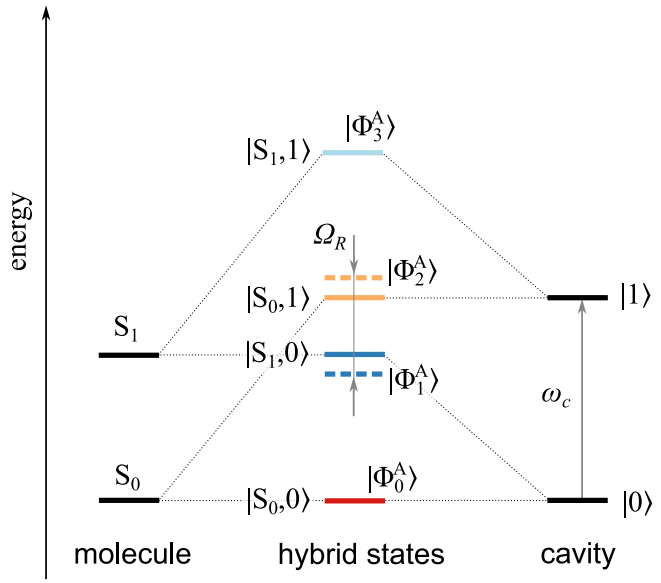

Fig. 2 | Jablonski diagram of molecular energy levels under strong molecule-cavity coupling regime. The polaritonic states emerge from the hybridization of the parent molecular electronic states with the photons with the frequency ω_c. For hybrid states, the solid and dashed lines represent the diabatic (or uncoupled) and adiabatic (or polaritonic) states, respectively. The Rabi splitting Ω_R is determined from the strength of the molecule-cavity coupling.

electromagnetic field of the photon becomes strong enough, hybridization between the electronic states and light occurs and hybrid light-matter quasiparticles, called polaritons, emerge[29,30]. The required strong light-matter interaction can be achieved, e.g., in optical cavities, such as the Fabry-Pérot cavity[31] or a plasmonic resonator[32]. The polaritonic states, emerging due to coupling of the cavity mode with the electronic states of organic chromophores mediated by the dipole moment $\boldsymbol{\mu}$ of the electronic transition, display characteristics markedly different from their parent states[33–38]. This offers a possibility for controlling the outcome of photochemical reactions in a non-intrusive and selective manner[33,38–43].

Here, we show that coupling to a photon mode in an optical cavity can considerably alter the photodynamics of a molecular motor and either inhibit or markedly slow down the motor's rotation. To introduce a strong coupling between a cavity photon mode with a LDRM described as a two-level molecular system[44–47], we use the Jaynes-Cummings (JC) model[29]. The electronic states of LDRM in the presence of the cavity mode are described by the spin-restricted ensemble-referenced Kohn-Sham (REKS) method[48,49] and its state-averaged (SA-REKS) and state-interaction (SI-SA-REKS, or SSR) variants[50–54] modified to accommodate the JC model[55]. The SSR/REKS method is used in a simplified density functional tight-binding (DFTB) formulation, i.e., DFTB/SSR, which enables one to study very large molecular systems at a very low computational cost[56–58]. In the following, the potential energy surfaces of the electronic and polaritonic states of the motor **1** in Fig. 1 are studied using the DFTB/SSR method in connection with the JC model[55]. In addition, a series of surface hopping-based nonadiabatic molecular dynamics simulations is carried out to investigate the effect of the cavity-molecule interaction on characteristics of the excited state decay in the motor **1**. It is demonstrated that coupling to a cavity mode detuned off-resonance from the vertical excitation energy of the motor markedly changes the quantum yield and lifetime of photoisomerization and represents, perhaps, the most efficient means for manipulating the motor's rotation using non-intrusive physical stimuli.

Results

Hybrid light-matter states, the polaritonic states, emerge in an optical cavity as the result of strong coupling between the cavity photon with the frequency ω_c and molecular electronic states under the regime where the coherent energy exchange between them is faster than the energy dissipation[29]. When the light-matter coupling is absent, i.e., when the coupling strength $g = 0$, the combined states of the cavity photons and molecular electronic states are given as simple direct products $|n,p\rangle = |n\rangle \otimes |p\rangle$, where n = S_0, S_1, ... labels the molecular electronic states and p = 0, 1, ... labels the states of p photons, see Fig. 2. Under the zero coupling, the diabatic (or uncoupled) states $|S_0,0\rangle$ and $|S_1,0\rangle$ are identical to the bare S_0 and S_1 states, and the $|S_0,1\rangle$ and $|S_1,1\rangle$ are replicas of the bare molecular states shifted upwards by the photon frequency ω_c.

When the molecular-photon interaction is turned on, i.e., $g \neq 0$ (by definition, $g = \sqrt{\frac{\hbar\omega_c}{2\epsilon_0 V_c}}$ where ω_c is the cavity photon frequency, ϵ_0 is the vacuum permittivity, and V_c is the effective mode volume of the cavity photon), the diabatic states closest in energy will mix and form new adiabatic polaritonic states $|\Phi_k^A\rangle$ (k = 0, 1, 2, 3). Usually, the cavity eigenmode ω_c is tuned to match the molecular vertical excitation energy, such that the $|S_1,0\rangle$ and $|S_0,1\rangle$ states become (nearly) degenerate and the adiabatic states $|\Phi_1^A\rangle$ and $|\Phi_2^A\rangle$ become their superpositions split by an energy gap known as the Rabi splitting Ω_R ($\Omega_R = 2\boldsymbol{\mu}\cdot\boldsymbol{\lambda}\sqrt{N}\hbar g$, where N is the number of molecules, $\boldsymbol{\mu}$ is the transition dipole moment, and $\boldsymbol{\lambda}$ is a unit vector along the field polarization). The other two diabatic states, $|S_0,0\rangle$ and $|S_1,1\rangle$, remain

unmodified because the interaction strength g is typically much smaller than the splitting between the bare energy levels.

Because the new $|\Phi_1^A\rangle$ and $|\Phi_2^A\rangle$ adiabatic states, also known as the lower (LP) and upper (UP) polaritonic states, are superpositions of the bare molecular $|S_0\rangle$ and $|S_1\rangle$ states, their potential energy surfaces (PESs) are strongly modified by the cavity-molecule interaction; especially in the regions where the diabatic $|S_1, 0\rangle$ and $|S_0, 1\rangle$ states were the closest in energy. The cavity-molecule interaction depends on the transition dipole moment between the S_1 and S_0 states (see the Methods section for details) and the modulation of molecular PESs becomes more pronounced in the geometries with large transition dipole.

The outlined JC model was implemented in connection with the DFTB/SSR method as described in ref. 55 and the PESs and non-adiabatic molecular dynamics (NAMD) of the motor **1** were studied using the LC-OC-DFTB/SSR method[55–58] (see the Methods section for detail). In the following, the analysis of the potential energy surfaces and dynamics will be presented for a zero field case (a free motor molecule outside the cavity), as well as for a few cases of cavity-molecule coupling, the resonant coupling and two off-resonant coupling scenarios, red-detuned and blue-detuned conditions[38]. In all cases, the forward, ZM → EP, and backward, EP → ZM, photoreactions are studied. The other two possible photoreactions in Fig. 1c (i.e., EM → ZP and ZP → EM) are identical with the former and involve the motor molecule rotated through 180° with respect to its original orientation. When reporting results of the simulations, the potential energy surfaces and trajectories are characterized in terms of two geometric parameters, the dihedral angle θ representing the torsion about the C_9=$C_{1'}$ bond (see Fig. 1a) and the pyramidalization angle ϕ at the C_9 atom[59]. First, the photoreactions will be investigated in the gas phase and a lossless optical cavity. Then, the effects of the environment and cavity losses will be simulated and analyzed. When simulating the effect of the environment, the possible interaction of the molecule with the metallic surface of the nanoplasmonic cavity is ignored. The use of a nanoplasmonic cavity is desirable for achieving magnitudes of the light-matter coupling strength sufficiently large for modifying the electronic states of the target molecule. The interaction with the cavity walls can be minimized by introducing insulating layers; to a certain degree, this can reduce the magnitude of the coupling with the cavity photons. These effects, however, are not considered here, and only the effect of the solvent present in the nanocavity is included.

Zero-coupling case in gas phase

As a reference for further comparisons, a zero-coupling (ZC, g = 0.0 a.u.) case was studied first in the gas phase; for solution phase calculations, see section "Effect of the environment". The profiles of the potential energy surfaces (PESs) of the ground S_0 and excited S_1 states along the dihedral angle θ are shown in Fig. 3. The PES profiles were obtained by constraining the central dihedral angle and optimizing all other geometric parameters in the ground electronic state. The excited state energies were obtained from the single-point calculations in the respective geometries. The stable (ZM) structure is lower in energy than the metastable (EP) structure by 0.086 eV (1.98 kcal/mol), which is in reasonable agreement with 2.04 kcal/mol obtained previously by Pang et al. with the use of the semiempirical OM2/MRCI method in the gas phase[60]. In addition, two minima occur in the excited state, which are characterized by different dihedral angles θ, 283.4° in ZM(S_1) and 254.3° in EP(S_1); see Supplementary Fig. 1 for the optimized structures. Near the torsion angle θ ~ 270°, two S_1/S_0 conical intersections are located, which are characterized by opposite values of the pyramidalization angle ϕ, −16.7° in CI_1 and +15.9° in CI_2; see insets in Fig. 3. The occurrence of these conical intersections is consistent with the results of Pang et al.[60] and with the previous theoretical works on a related molecular motor[61,62].

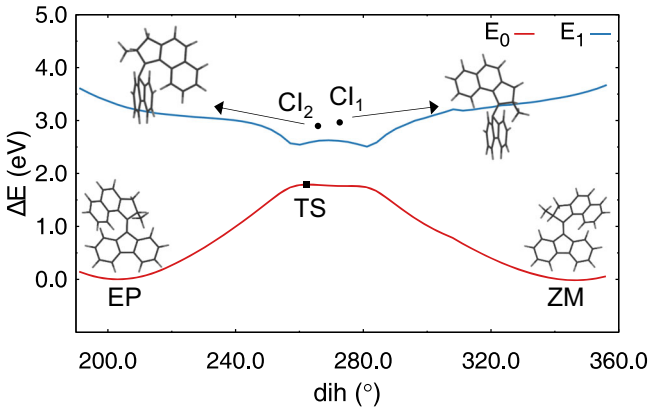

Fig. 3 | Profiles of the ground and excited PESs of the motor 1 along the dihedral angle θ in the absence of coupling with the cavity photon. The relaxed scan was obtained by constraining the dihedral (dih) angle in the ground electronic state. The insets show the structures of the ground state minima (ZM and EP) and the minimum energy conical intersections (MECI), CI_1 and CI_2, between the S_0 and S_1 states occurring near the dihedral angle θ ~ 270°. The pyramidalization and dihedral angles (ϕ, θ) for the ZM, CI_1, CI_2, and EP structures are (−1.39°, 345.8°), (−16.7°, 272.6°), (15.9°, 265.8°), and (−1.36°, 202.6°), respectively. The values (ϕ, θ) for the transition state (TS) structure are (−1.40°, 262.1°). Source data are provided as a Source Data file.

In addition to constrained optimization, minimum energy path (MEP) optimizations were performed for the ZM → EP, and EP → ZM photoreactions, which are shown in Supplementary Fig. 2. Starting from the Franck-Condon point of ZM or EP structure on the S_1 PES, the motor **1** approaches the S_1 minimum through a barrierless pathway by changing the central dihedral angle θ. Further relaxation occurs via CI_1 or CI_2, characterized by substantial pyramidalization distortion. Both conical intersections are energetically accessible from the Franck-Condon point. After reaching a conical intersection, the photoisomerization reaction switches to the S_0 state and completes the transformation along the dihedral angle degree of freedom. In addition, a transition state (TS) structure on the ground state PES was optimized (see Fig. 3 and Supplementary Fig. 3). For the motor **1**, the homolytic breaking of the central π-bond is favorable in the S_0 state, which results in the TS structure having the diradical (DIR) characteristics. In the S_1 state, the TS structure acquires the charge transfer (CT) character. Therefore, the conical intersections are accessed by pyramidalization distortion, which connects the DIR and CT structures[63]. The relative energies of all optimized structures are given in Supplementary Table 1.

The NAMD trajectories were initiated in the geometries obtained by Boltzmann sampling of the ground state trajectories ran for 20 ps with a time step of 0.5 fs under the velocity-rescaling thermostat at 300 K. In total, 100 NAMD trajectories were started in these geometries by populating initially the S_1 state and running the simulations for 5 ps with a time step of 0.5 fs under the NVE (or micro-canonical) ensemble conditions.

The resulting population dynamics during the ZM → EP and EP → ZM photoreactions are shown in Fig. 4. The average S_1 state lifetimes for both photoreactions are 2.75 ps for ZM → EP and 2.21 ps for EP → ZM. The obtained S_1 lifetime of the ZM → EP stage is considerably longer than ca. 710 fs obtained by Pang et al.[60] in the semiempirical OM2/MRCI simulations, and agrees better with the experimental estimates. Thus, Conyard et al. obtained 1.5 ± 0.3 ps for the exponential decay constant of the S_1 state that is populated a few hundred femtoseconds after the start of the ZM → EP photoreaction[64]. This suggests that the measured S_1 lifetime may vary in the range of 1.7–2.1 ps, which is in reasonable agreement with the lifetimes obtained here.

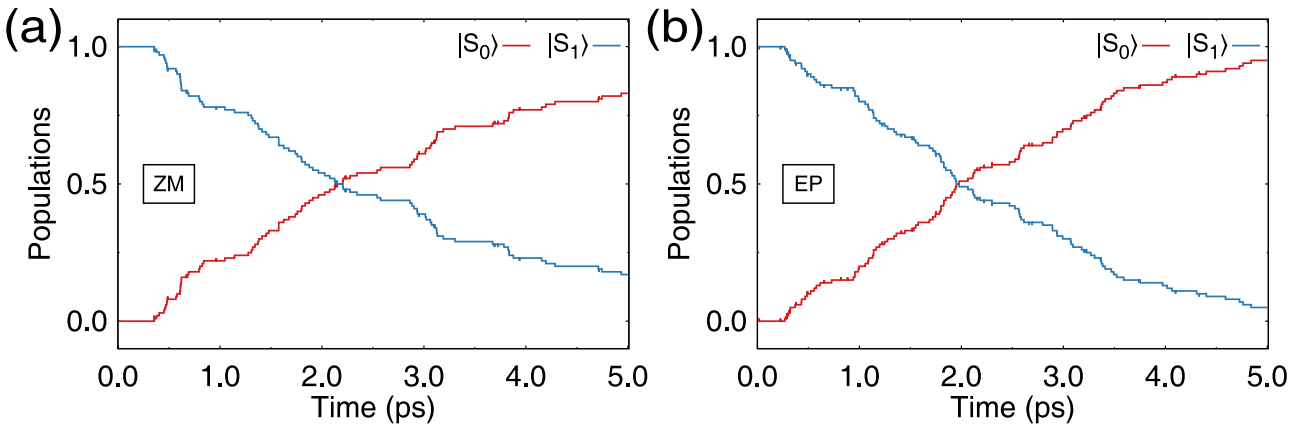

Fig. 4 | Time evolution of the populations of the electronic states in the zero-coupling case. a Population dynamics during the ZM → EP photoreaction. The red and blue curves show populations of the S_0 and S_1 states, respectively. **b** Population dynamics during the EP → ZM photoreaction. Source data are provided as a Source Data file.

Out of a hundred trajectories started for the ZM → EP and EP → ZM photoreactions, 83 and 95 trajectories have undergone the $S_1 \rightarrow S_0$ population transfer and the rest of the trajectories remained in the S_1 state at the end of the simulations (5 ps). For the ZM → EP photoreaction, 40 trajectories reached the EP structure on the S_0 PES, and 43 trajectories returned to the ZM structure, which corresponds to the quantum yield of 48.2%. This quantum yield (QY) is somewhat lower than 59.9% obtained by Pang et al. in their gas phase simulations[60]. The remaining difference with the experimental QY of 14%[65] is likely to be caused by solvent because the solvent molecules in the solvation shell do not have sufficient time to rearrange during the ultrafast photoisomerization and mainly keep the arrangement that favors the solute structure at the beginning of the photoreaction[66,67]. The effect of the environment is discussed in the section "Effect of the environment" below. For the EP → ZM photoreaction, the respective QY is 41.1% (39 trajectories ended in ZM and 56 returned to EP), which is marginally lower than in the ZM → EP photoreaction. Overall, the obtained characteristics of the ZM → EP and EP → ZM photoreactions of **1** are consistent with previous theoretical simulations[60].

Resonant strong coupling in gas-phase lossless optical cavity

Turning to non-zero coupling between the cavity mode and the molecule, the case of resonant coupling was studied first. For this case, the cavity mode frequency ω_c was tuned to the energy of the vertical electronic transition of the starting structures of the ZM → EP and EP → ZM photoreactions in their equilibrium ground state geometries. Therefore, $\hbar\omega_c$ was set to 3.54 eV for the ZM structure and to 3.3 eV for the EP structure. The coupling strength g was set to 0.001 a.u. and the electric field of the cavity mode was set parallel to the central C_9=$C_{1'}$ double bond. It is noteworthy that the transition dipole moment of the $S_1 \leftarrow S_0$ transition is almost perfectly parallel to the C_9=$C_{1'}$ bond for both structures, ZM and EP (see Supplementary Fig. 4).

The profiles of the polaritonic PESs (PPESs) of the ZM → EP and EP → ZM photoreactions along the central dihedral angle θ are shown in Fig. 5. The geometries of the ground state equilibrium structures and the profile of the ground polaritonic state $|\Phi_0^A\rangle$ remain in the SC case the same as in the ZC case. As seen in Fig. 2, the lowest polaritonic state $|\Phi_0^A\rangle$ is unaffected by the cavity-molecule interaction, and the characteristics of this state are the same as the ground electronic state. The same is true for the highest polaritonic state $|\Phi_3^A\rangle$, which replicates the profile of the uncoupled S_1 electronic state, which is now dressed by a single cavity photon, and its energy is translated upwards by the photon frequency.

The greatest alteration occurs for the lower polaritonic $|\Phi_1^A\rangle$ and the upper polaritonic $|\Phi_2^A\rangle$ states, which become superpositions of the uncoupled $|S_0, 1\rangle$ and $|S_1, 0\rangle$ states, i.e., $|\Phi_1^A\rangle \sim \frac{1}{\sqrt{2}}|S_0, 1\rangle + \frac{1}{\sqrt{2}}|S_1, 0\rangle$ and $|\Phi_2^A\rangle \sim \frac{1}{\sqrt{2}}|S_0, 1\rangle - \frac{1}{\sqrt{2}}|S_1, 0\rangle$, split due to the cavity-molecule interaction. The Rabi splitting Ω_R between the $|\Phi_1^A\rangle$ and $|\Phi_2^A\rangle$ states becomes 173 and 178 meV for the ZM and EP equilibrium structures, respectively. This corresponds to Ω_R on the order of a few percent (ca. 5%) of the vertical excitation energy of the motor, which is typical for the strong coupling regime. Note that, Ω_R exceeding ca. 20% of the molecular excitation energy implies the ultrastrong coupling regime, which is not addressed in this paper.

Although a noticeable modulation of the potential energy surfaces is seen near the ground state equilibrium geometries of the ZM and EP structures, no new local minima or transition states emerge on these surfaces. This implies that the dynamics of the motor in the resonant SC regime may not be very strongly affected by the cavity-molecule interaction. To verify this conjecture, a series of NAMD simulations have been carried out for the resonant SC regime. In these simulations, the same initial geometries as in the ZC case were used. In total, 100 trajectories were propagated for each photoreaction, ZM → EP and EP → ZM. At the beginning of the trajectories, the upper polaritonic state $|\Phi_2^A\rangle$ was populated, and the trajectories were propagated up to 5 ps with a timestep of 0.5 fs.

The population dynamics obtained for both photoreactions are shown in Fig. 6. In both photoreactions, the upper polaritonic state $|\Phi_2^A\rangle$ is rapidly (within less than 100 fs) depopulated, and its population is transferred to the lower polaritonic state $|\Phi_1^A\rangle$. The $|\Phi_2^A\rangle \rightarrow |\Phi_1^A\rangle$ decay begins immediately upon excitation and occurs with the decay constants of 42.7 and 35.7 fs for the ZM → EP and EP → ZM reactions, respectively. Upon the rapid initial population transfer, the $|\Phi_1^A\rangle$ state begins to slowly decay to the ground polaritonic state $|\Phi_0^A\rangle$, with a latency time of ca. 200–300 fs for both photoreactions. Analysis of the populations of the electronic states (see Supplementary Fig. 5) reveals that, at the beginning of the photoreaction, both electronic states S_1 and S_0 are equally populated due to the entanglement in the polaritonic states $|\Phi_2^A\rangle$ and $|\Phi_1^A\rangle$. The $|\Phi_2^A\rangle \rightarrow |\Phi_1^A\rangle$ decay results in a disentanglement of the electronic states, and the S_1 state becomes nearly fully populated within the first ca. 200–300 fs. Then, the S_1 population begins to decay to the ground electronic state due to the $|\Phi_1^A\rangle \rightarrow |\Phi_0^A\rangle$ transfer. The $|\Phi_1^A\rangle \rightarrow |\Phi_0^A\rangle$ population transfer follows exponential decay, with the lifetimes of 2.50 ps and 2.66 ps for the ZM → EP and EP → ZM reactions, respectively.

https://doi.org/10.1038/s41467-025-59607-3

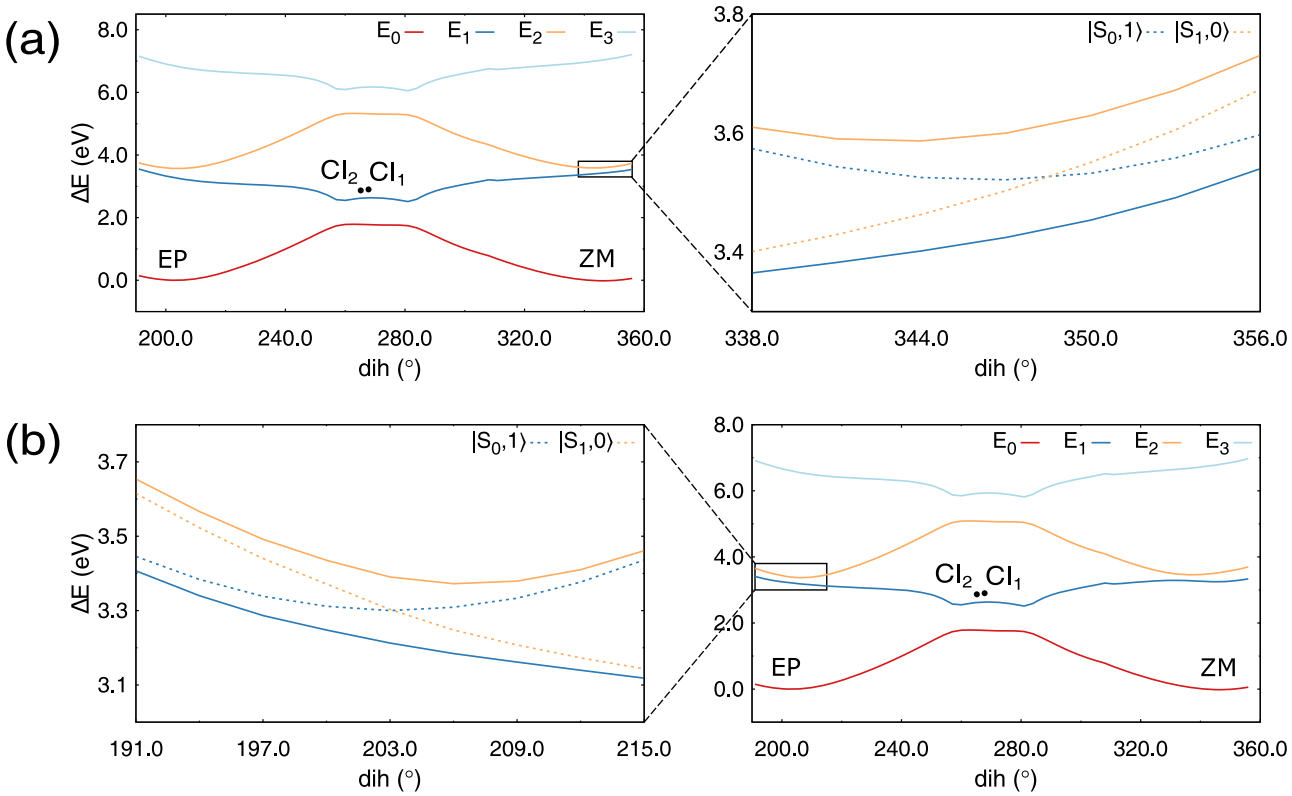

Fig. 5 | Potential energy curves of the motor 1 strongly coupled to a single cavity. a Profiles of polaritonic states along the dihedral (dih) angle θ for the ZM → EP photoreaction. The relaxed scan was obtained by constraining the dihedral angle in the ground polaritonic state. The cavity mode frequency is tuned to the vertical excitation energy of the ZM structure, i.e., 3.54 eV. The black dots in the main plot show the positions of two conical intersections, CI_1 and CI_2, between the $|\Phi_0^A\rangle$ and $|\Phi_1^A\rangle$ polaritonic states. The values (ϕ, θ) of the pyramidalization and dihedral angles of the ZM, CI_1, CI_2, and EP structures are (−1.39°, 345.8°), (−18.0°, 267.8°), (16.2°, 265.2°), and (−1.36°, 202.6°), respectively. The rectangular region in the main plot is magnified in the inset next to it. The dotted lines in the inset show the uncoupled states; see Fig. 2 for more detail. **b** The same for the EP → ZM photoreaction. The cavity mode is tuned to 3.3 eV, which corresponds to the vertical excitation energy of the EP structure. The values (ϕ, θ) of the pyramidalization and dihedral angles of the EP, CI_1, CI_2, and ZM structures are (−1.36°, 202.6°), (−18.0°, 267.8°), (16.2°, 265.2°), and (−1.39°, 345.8°), respectively. Note that the same range of the central dihedral angle θ is chosen in panels (a) and (b); which means that the ZM structure corresponds to $\theta \approx 360°$. Source data are provided as a Source Data file.

The latency in the $|\Phi_1^A\rangle \rightarrow |\Phi_0^A\rangle$ decay is caused by the necessity for the nuclear trajectories to reach structures in geometrical proximity of the $|\Phi_1^A\rangle/|\Phi_0^A\rangle$ conical intersections, which occur at the torsion angle θ near ca. 270°; see Fig. 5. Analysis of the geometries along the trajectories suggests that this occurs after approximately 700 fs since the start of the trajectories. By this time, the majority of trajectories reach the minimum on the $|\Phi_1^A\rangle$ PPES (see Fig. 6) and remain in its basin, slowly decaying to the $|\Phi_0^A\rangle$ state through the CI_1 and CI_2 intersections. Supplementary Fig. 6 shows a distribution of the number of trajectories approaching CI_1 or CI_2 at different instances of time. The majority of trajectories decay through CI_2, however (quasi-)periodic oscillations with a period of ≈1.0 ps are observed for the decay events through CI_2 and CI_1; see Supplementary Fig. 6. The relatively long period of oscillations between decays through CI_2 and CI_1 is caused by large variations in the pyramidalization angle needed to reach the respective CI seams. Similar oscillations caused by the wobbling of the central double bond during the dynamics have also been noticed in the previous NAMD simulations[61]. It is noteworthy that, during the dynamics, the orientation of the central C=C double bond on average remains the same as at the beginning of the photoreaction. This happens because the coupling with the cavity photon's electric field exerts a relatively low net force on the motor **1**, which remains predominantly aligned with the C=C bond direction. As seen in Supplementary Fig. 7, the polaritonic PESs remain essentially flat along the alignment angle, defined as the angle between the C=C bond and the cavity axis (see Fig. 1c).

During the 5 ps propagation time, 82 trajectories in the ZM → EP reaction and 87 trajectories in the EP → ZM reaction undergo the $|\Phi_1^A\rangle \rightarrow |\Phi_0^A\rangle$ population transfer. In the ZM → EP reaction, 50 trajectories move forward and produce the EP final structure and 32 trajectories turn back towards the ZM structure. The ratio of the productive to unproductive trajectories changes to 48:39 in the EP → ZM reaction. Therefore, the two photoreactions exhibit quantum yields of 61.0% (ZM → EP) and 55.2% (EP → ZM), which are not much different from the zero-field scenario; 48.2% and 41.1%, respectively. Given that the lifetimes of the $|\Phi_1^A\rangle \rightarrow |\Phi_0^A\rangle$ decay in the resonant SC case are almost the same as in the field-free case, we can conclude that the resonant coupling with a cavity mode does not considerably alter the characteristics of the ZM → EP and EP → ZM photoreactions.

JC model versus quantum Rabi model

So far the JC model has been used in our work, which uses the (low-frequency) rotating-wave approximation and neglects the effect of the (high-frequency) counter-rotating contribution. To evaluate the effect of the rotating-wave approximation, the potential energy surfaces and photodynamics of the two photoreactions of the motor **1** have been investigated with the use of the full quantum Rabi model, which includes the counter-rotating contributions; see the Methods section. The inclusion of the counter-rotating terms leads to coupling between the $|S_0, 0\rangle$ and $|S_1, 1\rangle$ diabatic states in the lowest polaritonic $|\Phi_0^A\rangle$ and highest polaritonic $|\Phi_3^A\rangle$ states. However, because the energy gap between the diabatic states is sufficiently wide, this results in only

https://doi.org/10.1038/s41467-025-59607-3

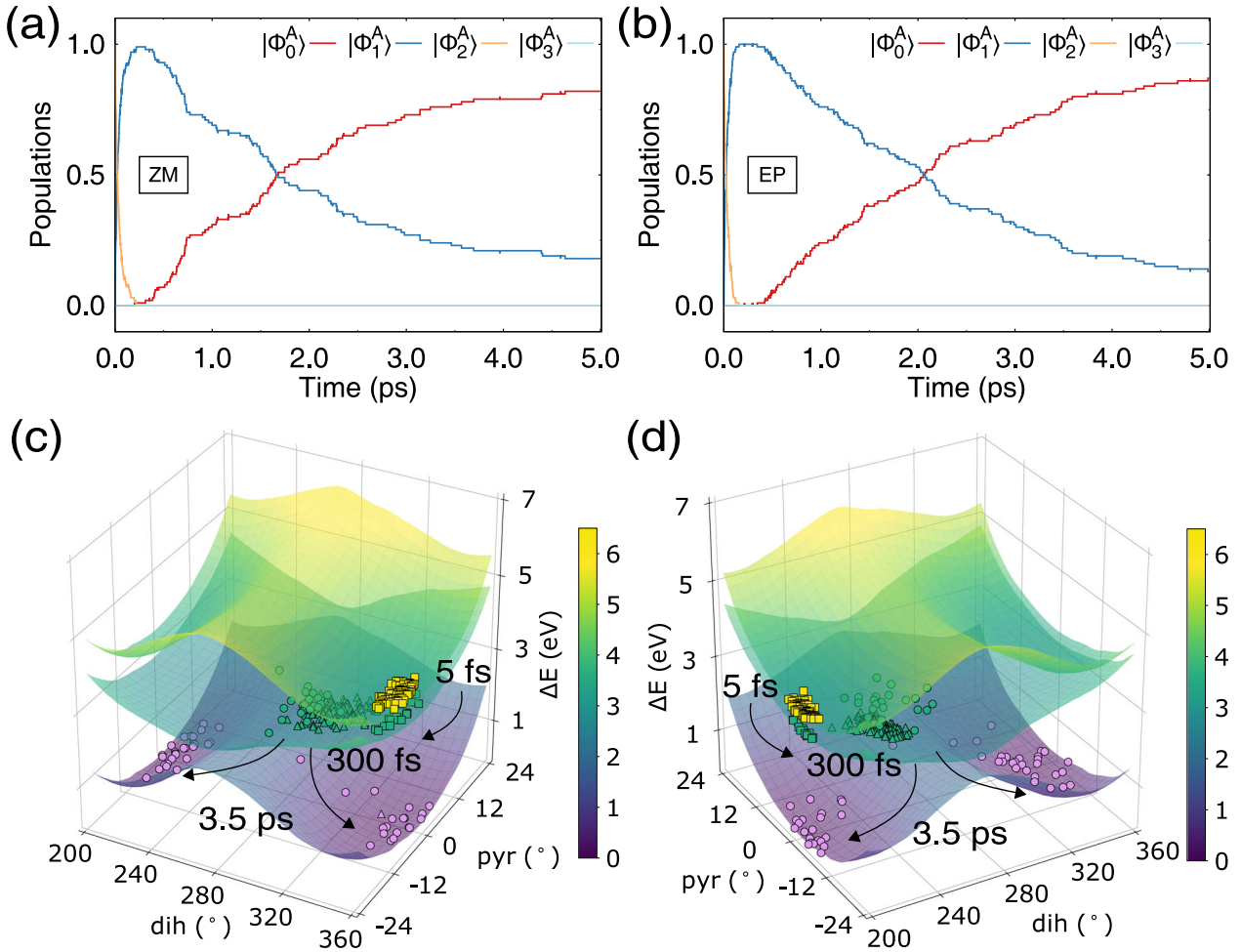

Fig. 6 | Time evolution of the populations of the polaritonic states in the resonant strong coupling case. a Population dynamics during the ZM → EP photoreaction. **b** Population dynamics during the EP → ZM photoreaction. **c** Location of the ZM → EP trajectories at specific instances of time shown on scanned surfaces of the upper polaritonic (yellowish colours) $|\Phi_2^A\rangle$ state, lower polaritonic (greenish colours) $|\Phi_1^A\rangle$ state, and the ground polaritonic (purplish colours) $|\Phi_0^A\rangle$ state with respect to the dihedral (dih) and pyramidalization (pyr) angles. The squares show trajectory points at 5 fs, the triangles at 300 fs, and the circles at 3.5 ps propagation time. The yellow markers show trajectories residing in the $|\Phi_2^A\rangle$ state, the green markers show trajectories in the $|\Phi_1^A\rangle$ state, and the purple markers the trajectories in the $|\Phi_0^A\rangle$ state. **d** The same for the EP → ZM photoreaction. Source data are provided as a Source Data file.

minor alteration of the dynamics and potential energy surfaces of the motor **1**. The profiles of the PPESs of the ZM → EP and EP → ZM photoreactions along the central dihedral angle θ are shown in Supplementary Fig. 8. The new $|\Phi_0^A\rangle$ and $|\Phi_3^A\rangle$ states are strongly dominated by the $|S_0, 0\rangle$ and $|S_1, 1\rangle$ diabatic states, respectively, which remain effectively uncoupled. Compared to the JC model (which neglects the counter-rotating term), similar equilibrium structures of the $|\Phi_0^A\rangle$ state and CIs between the $|\Phi_0^A\rangle$ and $|\Phi_1^A\rangle$ states are obtained in the quantum Rabi model.

In addition to studying the potential energy surfaces, 50 NAMD trajectories for both photoreactions were propagated for the Rabi model. Because the cavity-molecule interaction does not largely affect the lowest polaritonic $|\Phi_0^A\rangle$ state, the same initial sampling conditions as in the ZC case were used. The population dynamics obtained for both photoreactions are shown in Supplementary Fig. 9. The characteristics of both photoreactions with the use of the Rabi model are nearly the same as with the use of the JC model: The $|\Phi_2^A\rangle \rightarrow |\Phi_1^A\rangle$ decay occurs with the decay constants of 52.0 and 32.9 fs for the ZM → EP and EP → ZM reactions, respectively. After the initial population transfer, the $|\Phi_1^A\rangle$ state decays to the lowest polaritonic $|\Phi_0^A\rangle$ state, with the lifetimes of 2.36 and 2.84 ps for the ZM → EP and EP → ZM reactions, respectively. During the 5 ps propagation time, 44 trajectories in the ZM → EP reaction and 46 trajectories in the EP → ZM reaction undergo the $|\Phi_1^A\rangle \rightarrow |\Phi_0^A\rangle$ population transfer. In the former case, 26 trajectories reach the final EP structure and 18 trajectories turn back towards the ZM structure. The ratio of the productive to unproductive trajectories changes to 21:25 in the EP → ZM reaction. Therefore, the quantum yields of 59.1% and 45.7% for the two photoreactions are obtained, which are close to both the ZC case (48.2% and 41.1%) and to the SC case with the JC model (61.0% and 55.2%). This implies that the rotating-wave approximation used in the JC model is sufficiently accurate for our simulations and will be used in the rest of the work.

Off-resonant strong coupling case

The resonant SC scenario studied above results in a strong mixing between the $|S_0, 1\rangle$ and $|S_1, 0\rangle$ diabatic states in the upper and lower polaritonic states near the ground state equilibrium geometry of both structures, ZM and EP. Therefore, the lower polaritonic state $|\Phi_1^A\rangle$ retains the most prominent characteristics of the $|S_1, 0\rangle$ diabatic state, which has a pronounced slope in the direction of torsion about the central dihedral angle θ; see Fig. 5. Because the $|\Phi_2^A\rangle \rightarrow |\Phi_1^A\rangle$ population transfer occurs on an ultrafast timescale (less than ca. 50 fs) and is not accompanied by a noticeable change of the angle θ, the dynamics of the LP state $|\Phi_1^A\rangle$ begins on a surface strongly resembling the $|S_1, 0\rangle$ PES. As a consequence, with the resonant excitation, the dynamics of

the $|\Phi_1^A\rangle \rightarrow |\Phi_0^A\rangle$ decay shows characteristics very similar to the field-free (ZC) case; see Fig. 4.

Here, we would like to inspect whether detuning the cavity mode frequency off-resonance with the molecular vertical transition can result in a stronger modification of the polaritonic PESs and the ensuing dynamics. To address this question, we have undertaken a series of NAMD simulations with the cavity mode frequency ω_c red-detuned and blue-detuned by 1.0 eV off-resonance with the respective molecular vertical excitation energy. In the case of the ZM → EP photoreaction, this implies using ω_c of 2.54 (red-detuned) and 4.54 eV (blue-detuned), and for the EP → ZM photoreaction the ω_c values of 2.3 and 4.3 eV, respectively. The coupling strength g in all cases was kept at its value used in the resonant SC case; i.e., 0.001 a.u. All simulations with the off-resonant frequencies begin in the upper polaritonic state.

Figure 7 shows the results for the ZM → EP photoreaction, where the upper polaritonic state was populated at the start. In the red-detuned case ($\omega_c = 2.54$ eV), the mixing between the $|S_0, 1\rangle$ and $|S_1, 0\rangle$ diabatic states occurs in a region of the dihedral angle θ shifted ca. 35° away from the Franck-Condon (FC) region; see Fig. 7a. Near the FC geometry, the LP state $|\Phi_1^A\rangle$ is almost entirely equivalent to the $|S_0, 1\rangle$ diabatic state and there is a local minimum near $\theta \approx 346°$ (or −14°) separated from the local minima at ca. ~270° (or −90°) by a barrier, seen in Fig. 7a. A similar shape of the PPES profile is seen in Fig. 7a for the values of θ approaching the EP structure ($\theta < 270°$). It may therefore be expected that when undergoing the $|\Phi_2^A\rangle \rightarrow |\Phi_1^A\rangle$ population transfer, a substantial part of the population can be diverted toward the new local minimum and will remain in the $|\Phi_1^A\rangle$ polaritonic state for a prolonged time; thus, essentially, blocking isomerization of ZM to EP.

To verify this conjecture, we ran a series of NAMD simulations, which were set up in the same way as in the resonant SC case, with the sole difference that ω_c was now set to 2.54 eV. The time evolution of the polaritonic state populations is shown in Fig. 7c. As seen in the figure, the initial $|\Phi_2^A\rangle$ population is transferred to $|\Phi_1^A\rangle$ on an ultrafast timescale with a lifetime of 32.9 fs. Although at the start of the trajectories, the UP state is dominated by the S_1 contribution and the LP state by the S_0 contribution, the two polaritonic states very rapidly (~10 fs) become superpositions of the S_1 and S_0 electronic states, which become equally populated; see Supplementary Fig. 10a. The $|\Phi_2^A\rangle \rightarrow |\Phi_1^A\rangle$ population transfer results in a rapid decay of the S_1 population, which is transferred to the S_0 state. After that, for the whole duration of the simulations (5 ps), the populations remain in the $|\Phi_1^A\rangle$ state, which is dominated by the S_0 electronic state, and no rotation about the central double bond takes place. Therefore, an off-resonant red-detuning of the cavity mode has the potential to block the isomerization of the motor and its rotation.

In addition to simulations started in the upper polaritonic state $|\Phi_2^A\rangle$, a series of simulations where the lower polaritonic state $|\Phi_1^A\rangle$ was initially populated have been carried out. As shown in Supplementary Fig. 11, the change in the initial state does not lead to significant changes in the dynamics; the rotation of the motor **1** remains blocked due to the off-resonant red-detuned coupling.

A different picture of the dynamics is observed in the blue-detuned case ($\omega_c = 4.54$ eV); see Fig. 7b, d, and f. The $|S_0, 1\rangle$ diabatic state is shifted upwards considerably above the $|S_1, 0\rangle$ diabatic state, which effectively minimizes their mixing in the UP and LP states; see Fig. 7b. Consequently, when populating the $|\Phi_2^A\rangle$ state at the beginning of the simulations, where trajectories are localized in the well near ZM configuration due to the strong S_0 contribution (see also Supplementary Fig. 10b), very slow decay of its population ensues on a timescale much longer than the simulation time (5 ps); mainly due to the finite energy gap between the UP and LP states. Within the simulation time, only 22 trajectories (out of 100) undergo the $|\Phi_2^A\rangle \rightarrow |\Phi_1^A\rangle$ population transfer (78 remain in $|\Phi_2^A\rangle$), out of which 19 trajectories subsequently undergo population transfer to the ground $|\Phi_0^A\rangle$ polaritonic state and 3 remain in the $|\Phi_1^A\rangle$ state. The $|\Phi_1^A\rangle \rightarrow |\Phi_0^A\rangle$ transfer occurs essentially on the same timescale as in the field-free case because the $|\Phi_1^A\rangle$ polaritonic state is almost pure S_1 electronic state and $|\Phi_0^A\rangle$ is S_0 (see Supplementary Fig. 10b). As seen in Fig. 7d, the depletion of the $|\Phi_2^A\rangle$ population is comparable to the recovery of the $|\Phi_0^A\rangle$ population, accompanied by an intermittent population of the $|\Phi_1^A\rangle$ state. In the end, 10 trajectories reach the EP structure and 9 fall back to the ZM structure; which produces a quantum yield (52.6%) very close to the field-free case (48.2%). Although there is no complete blockade of the rotation as in the red-detuning case, the blue-detuning has the potential to slow down the photoisomerization process without strongly affecting its quantum yield.

In addition to simulations started in the upper polaritonic state, a series of simulations initiated in the lower polaritonic state have been carried out. Because the lower polaritonic state $|\Phi_1^A\rangle$ remains almost pure S_1 state, the dynamics typical for the field-free situation has been observed; see Supplementary Fig. 12. Therefore, in the blue-detuned scenario, the dynamics is strongly affected by the initial population of the polaritonic states.

Generally, a quite similar picture is observed in the off-resonant coupling simulations of the EP → ZM photoreaction; see Fig. 8. In the red-detuned case ($\omega_c = 2.3$ eV), the barrier on the $|\Phi_1^A\rangle$ PPES occurs at ca. 233° of torsion, near which the $|S_0, 1\rangle$ and $|S_1, 0\rangle$ diabatic states are strongly mixed; see Fig. 8a and Supplementary Fig. 10c. When starting in the fully populated $|\Phi_2^A\rangle$ state, the population evolves as shown in Fig. 8c, where it is seen that population transfer to the $|\Phi_1^A\rangle$ state occurs on a very rapid timescale of 21.8 fs. As shown in Supplementary Fig. 10c, this results in redistribution of the populations of the S_1 and S_0 electronic states, very similar to what was observed for the ZM → EP photoreaction. Upon the $|\Phi_2^A\rangle \rightarrow |\Phi_1^A\rangle$ transfer, the $|\Phi_1^A\rangle$ population decays on an extremely slow timescale, where only three trajectories undergo a transition to the ground state until the end of the simulations. Out of the three trajectories, two move forward to the ZM structure and one falls back to EP; which produces a (not statistically meaningful) quantum yield of 66.6%. Given that only three trajectories underwent transition to the ground state, it is very difficult to estimate the possible excited state lifetime in this case. However, it is plausible that the motor's rotation is blocked for a prolonged time.

The blue-detuned dynamics ($\omega_c = 4.3$ eV) during the EP → ZM photoreaction is, generally, similar to the ZM → EP case; see Fig. 8b, d, and f. The blue-detuning results in the UP and LP states, which are represented by nearly pure $|S_0, 1\rangle$ and $|S_1, 0\rangle$ diabatic states, see Fig. 8b and Supplementary Fig. 10d, and the dynamics shows characteristics very similar to the dynamics of the blue-detuned ZM → EP photoreaction. During the simulation time, 17 trajectories undergo population transfer to the $|\Phi_1^A\rangle$ state (83 remain in $|\Phi_2^A\rangle$), out of which nine trajectories go through to $|\Phi_0^A\rangle$; see Fig. 8d. Out of nine decayed trajectories, seven move forward to the ZM structure and two fall back to EP. Because the number of trajectories is too small, no meaningful comparison of the quantum yield of this reaction can be made. However, as in the ZM → EP case, one might expect that much longer simulations would produce a quantum yield in close agreement with the field-free case. Therefore, it can be conjectured that similar to the ZM → EP case, blue-detuning offers a means to flexibly adjust the excited state lifetime (hence, the speed of the motor's rotation) without strongly affecting the isomerization quantum yield.

Effect of the environment

So far, the simulations of the motor's dynamics were carried out in the gas phase. Although gas-phase optical cavities have recently emerged[68,69], the most widely used optical and plasmonic cavities are implemented in the condensed phase[32–38]. Therefore, it appears important to investigate the effect of the condensed-phase environment on the dynamics of the motor embedded in a cavity. Here, we follow the same logic as in the preceding sections and present the ZC, resonant SC, and off-resonant SC cases in a solvent (dichloromethane, DCM).

https://doi.org/10.1038/s41467-025-59607-3

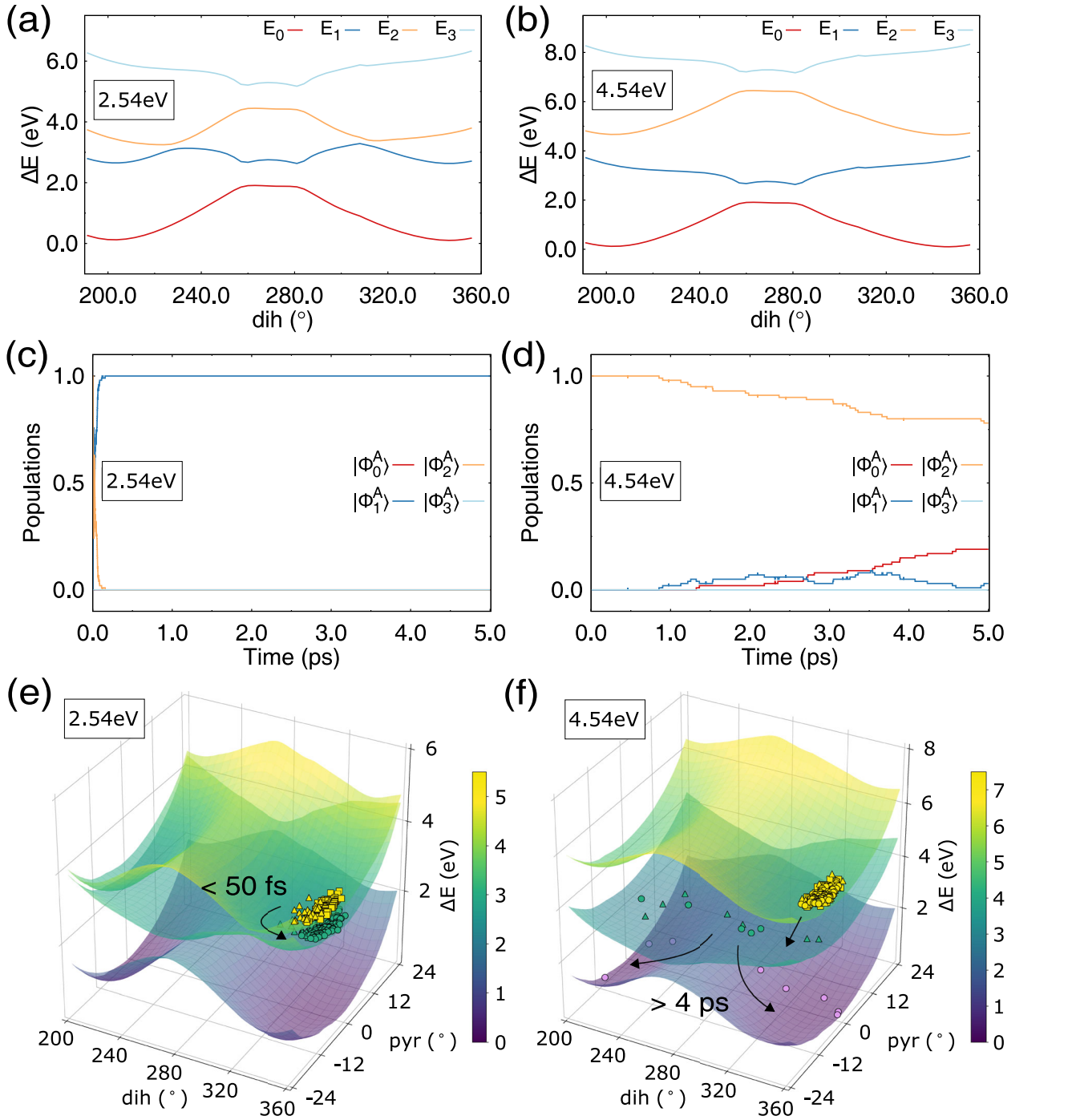

Fig. 7 | Potential energy surfaces and non-adiabatic population dynamics of the ZM → EP photoreaction in the off-resonant strong coupling case. a Polaritonic potential energy curves with respect to the dihedral angle θ and **c** time evolution of the populations of the polaritonic states for $\omega_c = 2.54$ eV. The relaxed scan was obtained by constraining the dihedral angle in the ground polaritonic state. **e** Location of the trajectories ($\omega_c = 2.54$ eV) at specific instances of time shown on scanned surfaces of the upper polaritonic (yellowish colours) $|\Phi_2^A\rangle$ state, lower polaritonic (greenish colours) $|\Phi_1^A\rangle$ state, and the ground polaritonic (purplish colours) $|\Phi_0^A\rangle$ state with respect to the dihedral (dih) and pyramidalization (pyr) angles. The squares show trajectory points at 5 fs, the triangles at 50 fs, and the circles at 2.4 ps propagation time. The yellow markers show trajectories residing in the $|\Phi_2^A\rangle$ state, the green markers show trajectories in the $|\Phi_1^A\rangle$ state, and the purple markers the trajectories in the $|\Phi_0^A\rangle$ state. **b**, **d**, and **f** The same for the cavity mode frequency $\omega_c = 4.54$ eV. The square, triangular, and circular markers in panel **f** show trajectory points at 5 fs, 2.0 ps, and 4.0 ps, respectively. Source data are provided as a Source Data file.

In ZC case, the dynamics of the motor **1** in the DCM solvent has been modeled by using the multiscale QM/MM approach, where the solute molecule is treated quantum mechanically and the solvent is described by an atomistic force field (see the Methods section for details). Because the experimental measurements on the motor **1** have been carried out in DCM solution, the same solvent is used in our simulations. The initial conditions for the QM/MM NAMD simulations have been prepared similarly to the gas-phase case, i.e., from Boltzmann sampling of the ground state trajectories running at 300 K for 30 ps with a time step of 0.5 fs under the velocity-rescaling thermostat. Using the initial sampling conditions, 50 NAMD trajectories have been propagated by populating initially the S_1 state and

https://doi.org/10.1038/s41467-025-59607-3

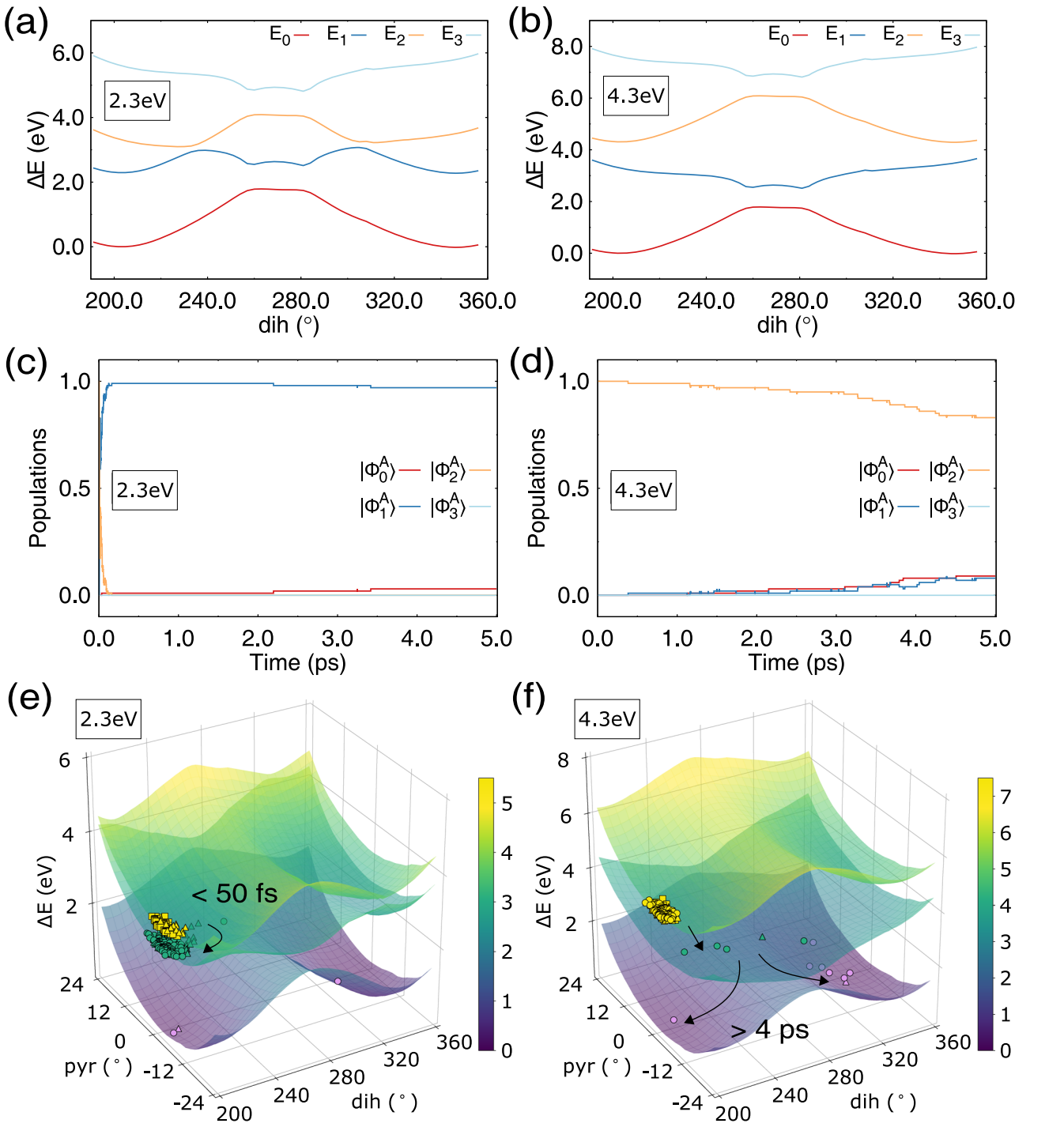

Fig. 8 | Potential energy surfaces and non-adiabatic population dynamics of the EP → ZM photoreaction in the off-resonant strong coupling case. a Polaritonic potential energy curves with respect to the dihedral angle θ and **c** time evolution of the populations of the polaritonic states for $\omega_c = 2.3$ eV. The relaxed scan was obtained by constraining the dihedral angle in the ground polaritonic state. **e** Location of the trajectories ($\omega_c = 2.3$ eV) at specific instances of time shown on scanned surfaces of the upper polaritonic (yellowish colours) $|\Phi_2^A\rangle$ state, lower polaritonic (greenish colours) $|\Phi_1^A\rangle$ state, and the ground polaritonic (purplish colours) $|\Phi_0^A\rangle$ state with respect to the dihedral (dih) and pyramidalization (pyr) angles. The squares show trajectory points at 5 fs, the triangles at 50 fs, and the circles at 2.4 ps propagation time. The yellow markers show trajectories residing in the $|\Phi_2^A\rangle$ state, the green markers show trajectories in the $|\Phi_1^A\rangle$ state, and the purple markers the trajectories in the $|\Phi_0^A\rangle$ state. **b**, **d**, and **f** The same for the cavity mode frequency $\omega_c = 4.3$ eV. The square, triangular, and circular markers in panel **f** show trajectory points at 5 fs, 2.0 ps, and 4.0 ps, respectively. Source data are provided as a Source Data file.

running for 6 ps with a time step of 0.5 fs under the NVE ensemble conditions.

Figure 9 shows the population dynamics for ZM → EP and EP → ZM photoreactions occurring in DCM solvent. Compared to the gas-phase simulations, the lifetime of the S_1 state becomes considerably longer than in the gas-phase simulations; it elongates from 2.75 ps and 2.21 ps for the ZM → EP and EP → ZM photoreactions, respectively, to 7.01 ps and 5.55 ps. The latter values were obtained by a monoexponential fit of the population curves and, because the population dynamics in Fig. 9 shows obvious non-exponential evolution, may be less precise

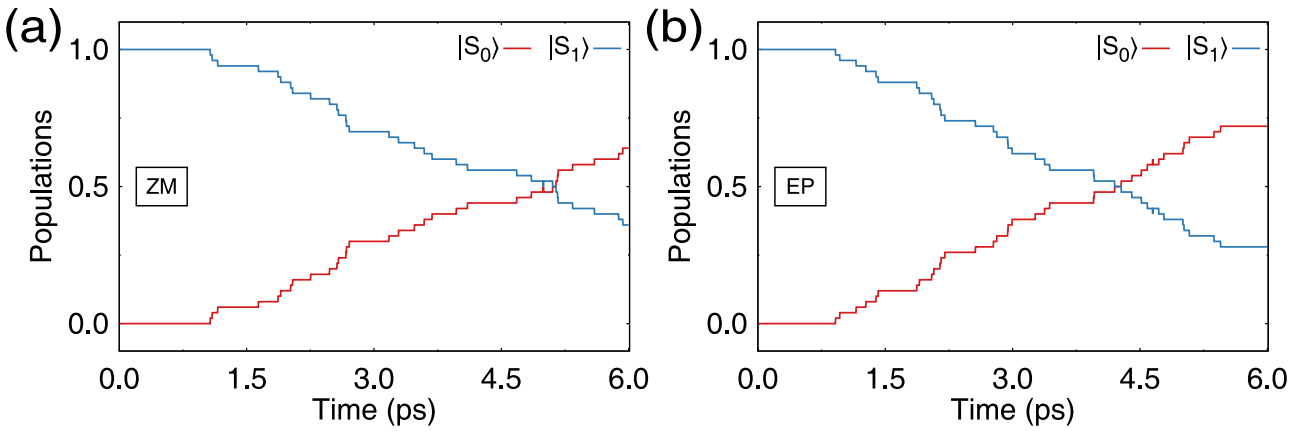

Fig. 9 | Time evolution of the populations of the electronic states in the presence of DCM solvent in the zero-coupling case. a Population dynamics during the ZM → EP photoreaction. The red and blue curves show populations of the S_0 and S_1 states, respectively. **b** Population dynamics during the EP → ZM photoreaction. Source data are provided as a Source Data file.

than in the gas-phase case. Our main focus, however, is on the quantum yield of the two photoreactions, which becomes markedly lower than in the gas-phase simulations. The QYs for the ZM → EP and EP → ZM photoreactions obtained in DCM solvent are 25.0% and 38.9%, respectively, and are in reasonable agreement with the experimental QYs of 14.0% and 50.0%[65]. The QY for EP → ZM is larger than for ZM → EP, which is consistent with the experimental observation. Although a relatively small number of trajectories (50) were propagated in our simulations, which may increase the margin of error for the obtained averages, it seems that the QM/MM simulations are capable of reasonably reproducing the experimental results reported in ref. 65.

To investigate the effect of the environment in an optical cavity on the characteristics of the photodynamics of the motor **1** in resonant SC case, a series of QM/MM NAMD simulations in DCM have been carried out. Although the actual environment in a cavity may be different, our main purpose is to find out whether the general conclusions drawn from the gas-phase simulations still hold in a condensed-phase setting. For the cavity mode frequency ω_c in resonance with the molecular vertical transitions, the same parameters as in the gas-phase simulations were used for the photon-molecule interaction. The initial conditions and the duration of the simulations are the same as in the field-free QM/MM simulations. The trajectories were started in the upper polaritonic state $|\Phi_2^A\rangle$ fully populated. Supplementary Fig. 13 shows the population dynamics for both photoreactions obtained in DCM solvent. Similar to the gas-phase resonant SC regime, the $|\Phi_2^A\rangle \rightarrow |\Phi_1^A\rangle$ decay is very rapid and occurs with the exponential decay constants of 51.5 and 81.3 fs for the ZM → EP and EP → ZM reactions, respectively. Upon the initial decay, the $|\Phi_1^A\rangle$ state slowly decays to the ground $|\Phi_0^A\rangle$ polaritonic state, with a latency time of ca. 500–700 fs for both photoreactions. The $|\Phi_1^A\rangle \rightarrow |\Phi_0^A\rangle$ population transfer follows exponential decay with the lifetimes of 5.29 and 4.41 ps for the ZM → EP and EP → ZM reactions, respectively, which are slightly faster than in the ZC case. During the 6 ps propagation time, 36 trajectories in the ZM → EP reaction and 39 trajectories in the EP → ZM reaction undergo the $|\Phi_1^A\rangle \rightarrow |\Phi_0^A\rangle$ population transfer, showing that the QYs are 22.2% and 30.8% for ZM → EP and EP → ZM reactions, respectively. Overall, the characteristics of the two photoreactions in the resonant SC regime do not differ substantially from the ZC case in the DCM solvent.

Similar to the gas-phase simulations, the red-detuned and blue-detuned scenarios were used for modeling the off-resonant strong molecule-cavity coupling. The population dynamics for the two scenarios is shown in Supplementary Fig. 14 for both photoreactions. In the red-detuned case, with ω_c = 2.54 or 2.3 eV for the ZM → EP and EP → ZM photoreactions, the initial $|\Phi_2^A\rangle$ population is transferred to $|\Phi_1^A\rangle$ with lifetimes of 29.6 and 32.7 fs, which is close to the gas-phase simulations. After the initial population transfer, the population of the $|\Phi_1^A\rangle$ state remains unchanged during the whole simulation time (6 ps), which implies that the isomerization of the motor **1** and its rotation is blocked by an off-resonant red-detuning of the cavity mode. In the off-resonant blue-detuned case, the QM/MM NAMD simulations predict that the initially populated $|\Phi_2^A\rangle$ state decays very slowly to the lower polaritonic $|\Phi_1^A\rangle$ state. The slow decay is caused by a wide gap between the UP and LP states. Within the simulation time (6 ps), out of 50 trajectories, only 4 trajectories in the ZM → EP reaction and 11 trajectories in the EP → ZM reaction undergo the $|\Phi_2^A\rangle \rightarrow |\Phi_1^A\rangle$ population transfer. Upon decaying to the $|\Phi_1^A\rangle$ state, the population transfer to the ground $|\Phi_0^A\rangle$ state occurs on a timescale similar to the field-free scenario. Overall, as in the resonant case, the characteristics of the ZM → EP and EP → ZM photoreactions obtained in the condensed-phase simulations are very similar to the gas-phase case, and the major conclusions drawn from the latter results remain unchanged.

Photoisomerization reaction with cavity losses

The results presented so far were obtained in a lossless cavity, and they do not take into account the possibility of photon loss in the cavity. While long cavity photon lifetimes were obtained within high-quality and gas-phase microcavities,[68–70] thus far mainly lossy plasmonic and optical microcavities have been used to achieve strong coupling with a single molecule[36,71]. Depending on the experimental setup, the photon lifetime in lossy cavities varies from a few dozen femtoseconds to nanoseconds,[72–79] and it seems important to include the effect of photon disappearance on the obtained dynamics.

Here, we investigate the effect of photon loss on the gas-phase dynamics of the polaritonic states using a Monte Carlo approach (see Methods section)[42,43]. In the following, the photodynamics of the motor **1** was analyzed using three different values for the photon lifetime: 10, 100, and 2000 fs. In particular, we examine whether the retardation of dynamics observed in the simulations in a lossless cavity holds in the case of photon loss. The major finding is that irrespective of the photon lifetime, the inhibition of the motor's rotation by resonant and off-resonant couplings takes place also in a lossy cavity.

In the case of strong resonant coupling, 100 gas-phase trajectories were replicated 10 times and post-processed for each lifetime, as described in the Methods section. Supplementary Figs. 15 and 16 show the population dynamics for both photoreactions, ZM → EP and EP → ZM, with cavity losses included, while Supplementary Fig. 17 represents the population projected on the electronic states S_0 and S_1. For the 2 ps photon lifetime, characteristics similar to a lossless cavity

have been obtained for both photoreactions. In the case of 100 fs photon lifetime, the population of the lower polaritonic state $|\Phi_1^A\rangle$ decreases markedly compared to the lossless case. The upper polaritonic to lower polaritonic state population transfer occurs on a faster timescale ($\lesssim$50 fs) and is not responsible for the depletion of the $|\Phi_1^A\rangle$ population. The latter depletion occurs due to a rapid loss of contribution from the $|S_0, 1\rangle$ diabatic state and collapse to the $|S_0, 0\rangle$ state as the result of photon disappearance. As a consequence, the population of the S_0 electronic state rises rapidly, as seen in Supplementary Fig. 17c and d. Furthermore, the QY of isomerization decreases to 43.3% and 40.0% for the ZM → EP and EP → ZM photoreactions, respectively. With the shortest (10 fs) photon lifetime, the population of the $|\Phi_1^A\rangle$ polaritonic state decreases even further, and the isomerization QY drops to 12.4% and 13.0% for the two photoreactions. Simultaneously with that, the ground state recovery time becomes noticeably faster, $\lesssim$1 ps; see Supplementary Figs. 15d and 16d. Therefore, there is a modulation of the motor's photodynamics in the resonant coupling case, mainly manifested in the decreasing quantum yield of photoisomerization.

In the resonant SC case, the influence of cavity losses on the dynamics of motor **1** isomerization is relatively modest due to the short lifetime of the upper polaritonic $|\Phi_2^A\rangle$ state. However, under strong off-resonant coupling conditions, the motor **1** remains for a prolonged time either in the $|\Phi_1^A\rangle$ state (red-detuned scenario) or in the $|\Phi_2^A\rangle$ state (blue-detuned scenario). In both situations, cavity losses can affect the dynamics, mainly due to the loss of the $|S_0, 1\rangle$ contribution in the polaritonic states and collapse to the ground electronic state.

For the red-detuned case of the ZM → EP photoreaction ($\omega_c = 2.54$ eV) and EP → ZM photoreaction ($\omega_c = 2.3$ eV), where 100 gas-phase trajectories were replicated 10 times for each photon lifetime, the population dynamics is shown in Supplementary Figs. 18 and 19. For all studied photon lifetimes, the $|\Phi_1^A\rangle \rightarrow |\Phi_0^A\rangle$ population transfer occurs within 5 ps. However, both polaritonic states, $|\Phi_1^A\rangle$ and $|\Phi_0^A\rangle$, contain a dominant contribution from the S_0 electronic state (see Supplementary Fig. 20) and, due to this, isomerization about the central double bond is inhibited and zero quantum yield of isomerization is obtained for all photon lifetimes. Therefore, an off-resonant red-detuning of the cavity mode blocks the photoisomerization and the motor's rotation regardless of the cavity lifetime.

A different picture of photodynamics is obtained in the blue-detuned case, where 100 gas-phase trajectories were replicated 10 times for each photon lifetime. Let us first discuss the ZM → EP photoreaction with the cavity photon $\omega_c = 4.54$ eV shown in Supplementary Fig. 21. In the lossless cavity case, the motor remained in the upper polaritonic $|\Phi_2^A\rangle$ state for a long time, which inhibited the rotation. With a lossy cavity, the $|\Phi_2^A\rangle$ state is strongly affected by the loss of the $|S_0, 1\rangle$ contribution and a collapse to the ground electronic state. Overall, a high S_0 contribution appears during 5 ps; see Supplementary Fig. 22. Although this reduces the UP state decay constant, the QY of rotation correlates approximately with the population of the LP state $|\Phi_1^A\rangle$. With all cavity lifetimes, the $|\Phi_1^A\rangle$ population does not exceed a few percent (3.2%), and the isomerization QY becomes $\lesssim$ 4.1%. Therefore, this effectively inhibits the motor's rotation.

Interestingly, lowering the cavity photon frequency can reinstate the motor's ability to isomerize, to a certain extent. Thus, Supplementary Figs. 23 and 24 show the population dynamics in a lossy cavity in blue-detuned cases with $\omega_c = 4.24$ and $\omega_c = 3.94$ eV, where 50 gas-phase trajectories were replicated 10 times for each photon lifetime. With $\omega_c = 4.24$ eV, a quantum yield of 24.5% is obtained with a cavity lifetime of 2 ps, which is lower than 61.0% in a lossless cavity. However, the shorter photon lifetimes, 100 and 10 fs, completely suppress the motor's rotation and result in a zero quantum yield. Using a lower frequency, cavity photon with $\omega_c = 3.94$ eV leads to the photoisomerization quantum yields of 57.0% ($\tau_c = 2$ ps), 12.9% (100 fs), and 0.0% (10 fs). Therefore, varying the cavity photon frequency in the blue-detuned case offers a handle for manipulating the motor's dynamics. Nevertheless, the main conclusion drawn from the lossless cavity simulations that blue-detuning can considerably slow down the motor's rotation remains valid for lossy cavities.

In the case of the inverse EP → ZM photoreaction, blue-detuning of the cavity photon leads to a very similar behavior as in the forward ZM → EP reaction. The population dynamics for the inverse photoreaction is shown in Supplementary Figs. 25, 26, and 27, for the cavity photon energies $\omega_c = 4.3$, 4.0, and 3.7 eV, respectively. Similar to the forward reaction, the quantum yield and excited state lifetime strongly depend on the photon's frequency, and rotation of the motor can be controlled by tuning ω_c and τ_c. Thus, using the 4.3 eV photon nearly completely blocks the rotation for all cavity photon lifetimes considered. With photons of lower energy, 4.0 and 3.7 eV, the rotation can be partly unfrozen, and the longest photon lifetime (2 ps) results in the largest isomerization quantum yield (21.8% and 43.1%), which remains markedly lower than in the field-free case (55.2%). Therefore, we can conclude that the inclusion of cavity losses does not invalidate the observations made for a lossless cavity, and varying the cavity photons characteristics, ω_c and τ_c, offers a means to control the motor's rotation. Furthermore, the cavity losses, typically viewed as harmful in polaritonic chemistry, provide here an additional means for manipulating the motor's dynamics; which also suggests that a photon leakage can be harnessed to benefit polaritonics.

Discussion

Here, we have addressed possible ways of in situ noninvasive manipulation of characteristics of the power stroke of LDRMs using stimuli orthogonal to the motor's source of energy. Towards this end, we have modeled the effect of strong coupling between the molecular ground and excited electronic states and a longitudinal mode of the photon in an optical cavity on the dynamics of excited state decay in the motor molecule. The NAMD simulations with the inclusion of strong cavity-molecule interaction through the use of the Jaynes-Cummings model revealed that: 1) In a lossless cavity, when the cavity mode frequency ω_c is in resonance with the molecular vertical excitation energy in the ground state equilibrium geometry ω_m, the characteristics of the ZM → EP and EP → ZM photoisomerization steps of the motor **1** (see Fig. 1) remain nearly the same as in the field-free case. However, the inclusion of the cavity losses modifies the dynamics and, when the loss of the cavity photon is sufficiently fast (10–100 fs), a considerable reduction of the photoreaction quantum yield is observed. 2) When a red-detuned ($\omega_c < \omega_m$) or a blue-detuned ($\omega_c > \omega_m$) cavity mode is employed, a dramatic change in the excited state lifetime and isomerization quantum yield of the motor is observed. 3) When the effect of the condensed-phase environment in a cavity on the characteristics of the photodynamics is included, the QM/MM simulations are capable of reasonably reproducing the experimental results.

The use of a red-detuned mode results in a (nearly) complete cessation of the motor's rotation about the central double bond. Under these conditions, the motor molecule remains in the lowest excited state for a considerably prolonged duration of time, which effectively blocks the motor's rotation both in a lossless optical cavity and a lossy plasmonic or optical cavity. With the blue-detuned cavity mode, the excited state lifetime increases by several orders of magnitude compared to the field-free case. However, this does not completely prevent the motor's rotation, and a very slow excited state decay, possibly close to a nanosecond timescale, is observed. Under the blue-detuning conditions, the motor **1** resides in the upper polaritonic state, which very slowly leaks its population to the lower polaritonic state. However, because the upper polaritonic state is

strongly affected by the photon disappearance due to cavity losses, the excited state lifetime and isomerization quantum yield become dependent on both the photon's frequency and lifetime. This offers a handle for manipulating the motor's rotation in a purely physical way.

Therefore, we believe that exploiting strong light-molecule interaction that takes place inside an optical cavity offers a flexible way of altering characteristics of the excited state decay in the molecule motor and its rotation speed. This prediction can be put to a test through experimental measurements; in particular, on gas-phase molecular polaritons, which are becoming possible at present[68].

Methods

Electronic structure calculations

The electronic ground (S_0) and lowest excited states (S_1) are obtained from LC-OC-DFTB/SSR(2,2) method[56,57] with ob2 parameters[80]. A new methodology, LC-OC-DFTB/SSR is developed by combining spin-restricted ensemble-referenced Kohn-Sham method[50–54] with density functional tight binding approach,[81–83] which can compute the excitation energies and conical intersection structures with high computational efficiency. An accuracy of the LC-OC-DFTB/SSR method is verified from several benchmark calculations with organic molecules and excited-state molecular dynamics simulations[56,57]. The atomic spin and onsite constants used for the calculation of the molecular motor are listed in Supplementary Table 2[57]. The transition dipole moments between the ground and lowest excited state and its derivatives with respect to the nuclear coordinate are obtained within LC-OC-DFTB/SSR formalism, which is essential for the stable propagation of nuclear dynamics[55]. All electronic structure calculations are performed using the development version of DFTB+ code[84]. To optimize the geometry of the ground and excited state minima, conical intersections, and minimum energy paths the DL-FIND package[85] was interfaced with the DFTB+ code.

Jaynes-Cummings model for polaritonic states

We used the Jaynes-Cummings (JC) model to perform the geometry optimization and the molecular dynamics simulation[29]. Here, we apply the Born-Oppenheimer approximation to separate the nuclear degree of freedom from the electronic and photonic degrees of freedom. The JC Hamiltonian with a lossless cavity mode is constructed as

$$\hat{H}_{\mathrm{JC}} = \hat{H}_{\mathrm{mol}} + \hat{H}_{\mathrm{ph}} + \hat{H}_{\mathrm{int}} \tag{1}$$

where $\hat{H}_{\mathrm{mol}}$ is the molecular electronic Hamiltonian. The cavity photon Hamiltonian $\hat{H}_{\mathrm{ph}}$ is expressed as $\hat{H}_{\mathrm{ph}} = \hbar\omega_c\left(\hat{a}_c^{\dagger}\hat{a}_c + 1/2\right)$ with the frequency for cavity mode ω_c. $\hat{a}_c^{\dagger}$ and $\hat{a}_c$ are the creation and annihilation operators of the cavity photon, respectively. The cavity-molecule interaction Hamiltonian $\hat{H}_{\mathrm{int}}$ under the dipole and rotating-wave approximations[86] is given by

$$\hat{H}_{\mathrm{int}} = g\boldsymbol{\mu}\cdot\boldsymbol{\lambda}\left(\hat{a}_c^{\dagger} + \hat{a}_c\right). \tag{2}$$

In eq. (2), g is the coupling strength, $\boldsymbol{\lambda}$ is the field polarization unit vector, and $\boldsymbol{\mu}$ is the transition dipole moment between the electronic states depending on the nuclear coordinate. The cavity-molecule system can be described in the basis of uncoupled state or product state $|n,p\rangle$ in the absence of the cavity-molecule interaction ($g = 0$), where $|n\rangle$ and $|p\rangle$ are the electronic and photonic states, respectively. We notice that four uncoupled states (i.e., $|S_0,0\rangle$, $|S_0,1\rangle$, $|S_1,0\rangle$, and $|S_1,1\rangle$) appear from two electronic states and a single cavity. The polaritonic states, which are obtained from diagonalization of the JC Hamiltonian including the cavity-molecule interaction[44], are expressed as linear combinations of the uncoupled states as $|\Phi_J^A\rangle = \sum_{n,p} U_{n,p}^J |n,p\rangle$ with the unitary matrix $U_{n,p}^J$. In the present case, $|\Phi_1^A\rangle$ and $|\Phi_2^A\rangle$ are referred to as lower polaritonic (LP) and upper polaritonic (UP) states, respectively, in which the contributions of the $|S_0,1\rangle$ and $|S_1,0\rangle$ diabatic states are determined by the coupling strength g. When going beyond the rotating-wave approximation and including the counter-rotating terms into the cavity-molecule interaction Hamiltonian, i.e., switching to the quantum Rabi model[87,88], the $|S_0,0\rangle$ and $|S_1,1\rangle$ diabatic states will also make contributions to the polaritonic states, which can affect the dynamics. Here, we used both the JC and quantum Rabi models to analyze the cavity-molecule interaction under the SC regime.

Non-adiabatic dynamics simulations

In the surface hopping based on the exact factorization (SHXF) dynamics with the polaritonic states, the nuclei move on a running polaritonic state, and the wavepacket motion is represented by a swarm of independent classical nuclear trajectories. To propagate the electronic wavefunction, the derivatives of the unitary matrix must be evaluated. However, it is numerically difficult to compute the derivative of the unitary matrix, since the unitary matrix is not uniquely defined. Instead, the electrons are propagated on the uncoupled state, which is somewhat similar to the local diabatization scheme proposed by Granucci et al.[89]; see ref. 55 for detailed equations of electronic propagation. The integration of the wavefunction coefficients is performed using the exponential propagator for stable norm conservation of the electrons. The hopping probabilities between the polaritonic states are calculated according to Tully's surface hopping algorithm[90]. The decoherence effect in the SHXF method is naturally introduced by the electron-nuclear correlation in the electronic equation of motion[91–97].

The gradients of the running polaritonic state are obtained by including both Hellmann-Feynman and Pulay contributions[98–100]. The Pulay force originating from the geometric dependence of the basis set is essential for accurate propagation of the nuclei[55]. Similarly, the polaritonic non-adiabatic coupling vectors, which can be used to compute the hopping probabilities and adjust the velocities upon hopping, are evaluated for every time step. We use the LC-OC-DFTB/SSR method to deal with contributions arising from the cavity-molecule interaction in the JC model. All calculations including the JC model with a lossless cavity mode and the non-adiabatic dynamics simulations were performed using PyUNIxMD program[101,102].

Quantum mechanics/molecular mechanics approach

To deal with the effects of the environment on the molecular motor system, we used the quantum mechanics/molecular mechanics (QM/MM) approach interfaced with the LC-OC-DFTB/SSR method. The molecular Hamiltonian $\hat{H}_{\mathrm{mol}}$ at the QM/MM level is given by

$$\hat{H}_{\mathrm{mol}} = \hat{H}_{\mathrm{QM}}(I) + \hat{H}_{\mathrm{MM}}(I+O) - \hat{H}_{\mathrm{MM}}(I) \tag{3}$$

where I and O indicate inner and outer subsystems, respectively, in the subtractive scheme. The inner subsystem is composed of the motor **1** (47 atoms) and the outer subsystem consists of 244 DCM molecules (1220 atoms) in a cubic cell with a size of $30 \times 30 \times 30$ Å^3. We neglect the charge-charge interaction in the QM/MM simulations because the nonpolar solvent (DCM) was used in the experiments[65]. The Lennard-Jones potential was considered for non-bonding interactions between the inner and outer subsystems. All-atom optimized potentials for liquid simulations (OPLS-AA) force field was used to evaluate the energies and forces at the MM level[103]. The QM/MM interface is implemented in the PyUNIxMD program[101], and all MM calculations are performed using the Tinker program[104].

Cavity losses

Following ref. 42, the cavity losses are included through a Monte Carlo scheme applied as a post-processing step over the trajectories executed in a lossless cavity. This approach is an approximation to the explicit inclusion of the cavity losses during the dynamics, see ref. 43.

The photon loss is treated as a stochastic event, the probability of which is evaluated at each timestep of the original trajectory. The latter probability P_{loss} is evaluated as

$$P_{\text{loss}}(t) = \frac{\Delta t}{\tau_c} |U^J_{S_0,1}(t)|^2, \quad (4)$$

where Δt is the time interval, τ_c is the photon lifetime, and $U^J_{S_0,1}$ is the coefficient of the diabatic state $|S_0, 1\rangle$ in the J-th polaritonic state at a given time t. Each of the original trajectories (50 or 100, see above) is replicated 10 times, and the obtained pool of trajectories is rerun, such that the statistical properties are obtained from 500 or 1000 trajectories, in each case. By comparing a random number in the [0, 1] interval with the decay probability P_{loss} at each time step, the collapse of the running polaritonic state to the $|S_0, 0\rangle$ state is defined, and the trajectory is stopped. In the present work, three different lifetimes of 10, 100, and 2000 fs were used, which cover a range of values appropriate for plasmonic and optical cavities.

Data availability

The data generated in this study are provided in this paper, and the Supplementary Information. Source data are provided in a Zenodo repository (https://doi.org/10.5281/zenodo.15239830).

Code availability

PyUNIxMD program is an open-source program under the MIT license, and can be found on public repository at https://github.com/skmin-lab/unixmd. The development version of DFTB+ used for this publication can be found on GitHub at https://github.com/inseonglee/dftbplus/tree/tdpGradReks.

References

1. Koumura, N., Zijlstra, R. W. J., van Delden, R. A., Harada, N. & Feringa, B. L. Light-driven monodirectional molecular rotor. *Nature* **401**, 152–155 (1999).
2. Koumura, N., Geertsema, E. M., van Gelder, M. B., Meetsma, A. & Feringa, B. L. Second generation light-driven molecular motors. unidirectional rotation controlled by a single stereogenic center with near-perfect photoequilibria and acceleration of the speed of rotation by structural modification. *J. Am. Chem. Soc.* **124**, 5037–5051 (2002).
3. Pollard, M. M., Meetsma, A. & Feringa, B. L. A redesign of light-driven rotary molecular motor. *Org. Biomol. Chem.* **6**, 507–512 (2008).
4. Credi, A. Artificial molecular motors powered by light. *Aust. J. Chem.* **59**, 157–169 (2006).
5. Balzani, V., Credi, A. & Venturi, M. Light powered molecular machines. *Chem. Soc. Rev.* **38**, 1542–1550 (2009).
6. Roke, D., Wezenberg, S. J. & Feringa, B. L. Molecular rotary motors: Unidirectional motion around double bonds. *Proc. Natl. Acad. Sci.* **115**, 9423–9431 (2018).
7. García-López, V., Liu, D. & Tour, J. M. Light-activated organic molecular motors and their applications. *Chem. Rev.* **120**, 79–124 (2020).
8. Corra, S., Curcio, M. & Credi, A. Photoactivated artificial molecular motors. *JACS Au* **3**, 1301–1313 (2023).
9. Liu, D. et al. Near-infrared light activates molecular nanomachines to drill into and kill cells. *ACS Nano* **13**, 6813–6823 (2019).
10. Ayala Orozco, C. et al. Visible-light-activated molecular nanomachines kill pancreatic cancer cells. *ACS Appl. Mater. Interfaces* **12**, 410–417 (2020).
11. Gunasekera, R. S. et al. Molecular nanomachines can destroy tissue or kill multicellular eukaryotes. *ACS Appl. Mater. Interfaces* **12**, 13657–13670 (2020).
12. Zheng, Y. et al. Optoregulated force application to cellular receptors using molecular motors. *Nat. Commun.* **12**, 3580 (2021).
13. Zhu, Q. et al. Multistate switching of spin selectivity in electron transport through light-driven molecular motors. *Adv. Sci.* **8**, 2101773 (2021).
14. Santos, A. L. et al. Light-activated molecular machines are fast-acting broad-spectrum antibacterials that target the membrane. *Sci. Adv.* **8**, eabm2055 (2022).
15. Lan, R. et al. Amplifying molecular scale rotary motion: The marriage of overcrowded alkene molecular motor with liquid crystals. *Adv. Mater.* **34**, 2109800 (2022).
16. Stähler, C. et al. Light-driven molecular motors embedded in covalent organic frameworks. *Chem. Sci.* **13**, 8253–8264 (2022).
17. Gao, C., Vargas Jentzsch, A., Moulin, E. & Giuseppone, N. Light-driven molecular whirligig. *J. Am. Chem. Soc.* **144**, 9845–9852 (2022).
18. Pooler, D. R. S., Lubbe, A. S., Crespi, S. & Feringa, B. L. Designing light-driven rotary molecular motors. *Chem. Sci.* **12**, 14964–14986 (2021).
19. Pollard, M. M., Klok, M., Pijper, D. & Feringa, B. L. Rate acceleration of light-driven rotary molecular motors. *Adv. Func. Mater.* **17**, 718–729 (2007).
20. Faulkner, A., van Leeuwen, T., Feringa, B. L. & Wezenberg, S. J. Allosteric regulation of the rotational speed in a light-driven molecular motor. *J. Am. Chem. Soc.* **138**, 13597–13603 (2016).
21. Wezenberg, S. J., Chen, K.-Y. & Feringa, B. L. Visible-light-driven photoisomerization and increased rotation speed of a molecular motor acting as a ligand in a ruthenium(ii) complex. *Angew. Chem. Int. Ed.* **54**, 11457–11461 (2015).
22. Ruangsupapichat, N., Pollard, M. M., Harutyunyan, S. R. & Feringa, B. L. Reversing the direction in a light-driven rotary molecular motor. *Nat. Chem.* **3**, 53–60 (2011).
23. Pfeifer, L. et al. Controlling forward and backward rotary molecular motion on demand. *Nat. Commun.* **13**, 2124 (2022).
24. Gisbert, Y., Fellert, M., Stindt, C. N., Gerstner, A. & Feringa, B. L. Molecular motors' magic methyl and its pivotal influence on rotation. *J. Am. Chem. Soc.* **146**, 12609–12619 (2024).
25. Qu, D.-H. & Feringa, B. L. Controlling molecular rotary motion with a self-complexing lock. *Angew. Chem. Int. Ed.* **49**, 1107–1110 (2010).
26. van Leeuwen, T. et al. Braking of a light-driven molecular rotary motor by chemical stimuli. *Chem. Eur. J.* **24**, 81–84 (2018).
27. Stindt, C. N. et al. Activating a light-driven molecular motor by metal complexation. *Chem* **9**, 2337–2348 (2023).
28. Einstein, A. Strahlungs-emission und absorption nach der quantentheorie. *Verh. der D. Physikal. Ges.* **18**, 318–323 (1916).
29. Jaynes, E. & Cummings, F. Comparison of quantum and semi-classical radiation theories with application to the beam maser. *Proc. IEEE* **51**, 89–109 (1963).
30. Agranovich, V., Benisty, H. & Weisbuch, C. Organic and inorganic quantum wells in a microcavity: Frenkel-wannier-mott excitons hybridization and energy transformation. *Solid State Commun.* **102**, 631–636 (1997).
31. Fabry, C. & Pérot, A. Theorie et applications d'une nouvelle methode de spectroscopie interferentielle. *Ann. Chim. Phys.* **16**, 115–144 (1899).
32. Gonçalves, M. R., Minassian, H. & Melikyan, A. Plasmonic resonators: fundamental properties and applications. *J. Phys. D: Appl. Phys.* **53**, 443002 (2020).
33. Ribeiro, R. F., Martínez-Martínez, L. A., Du, M., Campos-Gonzalez-Angulo, J. & Yuen-Zhou, J. Polariton chemistry: controlling molecular dynamics with optical cavities. *Chem. Sci.* **9**, 6325–6339 (2018).

34. Zeng, H. et al. Control of photoswitching kinetics with strong light-matter coupling in a cavity. *J. Am. Chem. Soc.* **145**, 19655–19661 (2023).
35. Flick, J., Ruggenthaler, M., Appel, H. & Rubio, A. Atoms and molecules in cavities, from weak to strong coupling in quantum-electrodynamics (qed) chemistry. *Proc. Natl. Acad. Sci.* **114**, 3026–3034 (2017).
36. Feist, J., Galego, J. & Garcia-Vidal, F. J. Polaritonic chemistry with organic molecules. *ACS Photonics* **5**, 205–216 (2018).
37. Hirai, K., Hutchison, J. A. & Uji-i, H. Molecular chemistry in cavity strong coupling. *Chem. Rev.* **123**, 8099–8126 (2023).
38. Bhuyan, R. et al. The rise and current status of polaritonic photochemistry and photophysics. *Chem. Rev.* **123**, 10877–10919 (2023).
39. Schwartz, T., Hutchison, J. A., Genet, C. & Ebbesen, T. W. Reversible switching of ultrastrong light-molecule coupling. *Phys. Rev. Lett.* **106**, 196405 (2011).
40. Hutchison, J. A., Schwartz, T., Genet, C., Devaux, E. & Ebbesen, T. W. Modifying chemical landscapes by coupling to vacuum fields. *Angew. Chem. Int. Ed.* **51**, 1592–1596 (2012).
41. Thomas, A. et al. Ground-state chemical reactivity under vibrational coupling to the vacuum electromagnetic field. *Angew. Chem. Int. Ed.* **55**, 11462–11466 (2016).
42. Fregoni, J., Granucci, G., Coccia, E., Persico, M. & Corni, S. Manipulating azobenzene photoisomerization through strong light-molecule coupling. *Nat. Commun.* **9**, 4688 (2018).
43. Fregoni, J., Granucci, G., Persico, M. & Corni, S. Strong coupling with light enhances the photoisomerization quantum yield of azobenzene. *Chem* **6**, 250–265 (2020).
44. Galego, J., Garcia-Vidal, F. J. & Feist, J. Cavity-induced modifications of molecular structure in the strong-coupling regime. *Phys. Rev. X* **5**, 041022 (2015).
45. Zhang, Y., Nelson, T. & Tretiak, S. Non-adiabatic molecular dynamics of molecules in the presence of strong light-matter interactions. *J. Chem. Phys.* **151**, 154109 (2019).
46. Fregoni, J., Corni, S., Persico, M. & Granucci, G. Photochemistry in the strong coupling regime: A trajectory surface hopping scheme. *J. Comp. Chem.* **41**, 2033–2044 (2020).
47. Rana, B., Hohenstein, E. G. & Martínez, T. J. Simulating the excited-state dynamics of polaritons with ab initio multiple spawning. *J. Phys. Chem. A* **128**, 139–151 (2024).
48. Filatov, M. & Shaik, S. A spin-restricted ensemble-referenced kohn-sham method and its application to diradicaloid situations. *Chem. Phys. Lett.* **304**, 429–437 (1999).
49. Moreira, Id. P. R., Costa, R., Filatov, M. & Illas, F. Restricted ensemble-referenced kohn-sham versus broken symmetry approaches in density functional theory: Magnetic coupling in cu binuclear complexes. *J. Chem. Theory Comput.* **3**, 764–774 (2007).
50. Kazaryan, A., Heuver, J. & Filatov, M. Excitation energies from spin-restricted ensemble-referenced kohn-sham method: A state-average approach. *J. Phys. Chem. A* **112**, 12980–12988 (2008).
51. Filatov, M. Assessment of density functional methods for obtaining geometries at conical intersections in organic molecules. *J. Chem. Theory Comput.* **9**, 4526–4541 (2013).
52. Filatov, M. Spin-restricted ensemble-referenced kohn-sham method: basic principles and application to strongly correlated ground and excited states of molecules. *WIREs Comput. Mol. Sci.* **5**, 146–167 (2015).
53. Filatov, M., Huix-Rotllant, M. & Burghardt, I. Ensemble density functional theory method correctly describes bond dissociation, excited state electron transfer, and double excitations. *J. Chem. Phys.* **142**, 184104 (2015).
54. Filatov, M. In *Ensemble dft approach to excited states of strongly correlated molecular systems* (eds Ferré, N., Filatov, M. & Huix-Rotllant, M.) *Density-functional methods for excited states*, Vol. 368 of *Top. Curr. Chem.* 97–124 (Springer, Heidelberg, 2016).
55. Lee, I. S., Filatov, M. & Min, S. K. Formulation of transition dipole gradients for non-adiabatic dynamics with polaritonic states. *J. Chem. Phys.* **160**, 154103 (2024).
56. Lee, I. S., Filatov, M. & Min, S. K. Formulation and implementation of the spin-restricted ensemble-referenced kohn-sham method in the context of the density functional tight binding approach. *J. Chem. Theory Comput.* **15**, 3021–3032 (2019).
57. Lee, I. S. & Min, S. K. Generalized formulation of the density functional tight binding-based restricted ensemble kohn-sham method with onsite correction to long-range correction. *J. Chem. Theory Comput.* **18**, 3391–3409 (2022).
58. Kim, T. I., Lee, I. S., Kim, H. & Min, S. K. Calculation of exciton couplings based on density functional tight-binding coupled to state-interaction state-averaged ensemble-referenced Kohn-Sham approach. *J. Chem. Phys.* **158**, 044106 (2023).
59. Haddon, R. C. Comment on the relationship of the pyramidalization angle at a conjugated carbon atom to the σ bond angles. *J. Phys. Chem. A* **105**, 4164–4165 (2001).
60. Pang, X. et al. "watching" the dark state in ultrafast nonadiabatic photoisomerization process of a light-driven molecular rotary motor. *J. Phys. Chem. A* **121**, 1240–1249 (2017).
61. Kazaryan, A. et al. Understanding the dynamics behind the photoisomerization of a light-driven fluorene molecular rotary motor. *J. Phys. Chem. A* **114**, 5058–5067 (2010).
62. Kazaryan, A., Lan, Z., Schäfer, L. V., Thiel, W. & Filatov, M. Surface hopping excited-state dynamics study of the photoisomerization of a light-driven fluorene molecular rotary motor. *J. Chem. Theory Comput.* **7**, 2189–2199 (2011).
63. Filatov, M. & Olivucci, M. Designing conical intersections for light-driven single molecule rotary motors: From precessional to axial motion. *J. Org. Chem.* **79**, 3587–3600 (2014).
64. Conyard, J. et al. Ultrafast dynamics in the power stroke of a molecular rotary motor. *Nat. Chem.* **4**, 547–551 (2012).
65. Conyard, J., Cnossen, A., Browne, W. R., Feringa, B. L. & Meech, S. R. Chemically optimizing operational efficiency of molecular rotary motors. *J. Am. Chem. Soc.* **136**, 9692–9700 (2014).
66. FilatovGulak, M. et al. Towards the engineering of a photon-only two-stroke rotary molecular motor. *Nat. Commun.* **13**, 6433 (2022).
67. FilatovGulak, M. et al. Impact of solvation on the photoisomerisation dynamics of a photon-only rotary molecular motor. *Commun. Phys.* **7**, 219 (2024).
68. Nelson, J. C. & Weichman, M. L. More than just smoke and mirrors: Gas-phase polaritons for optical control of chemistry. *J. Chem. Phys.* **161**, 074304 (2024).
69. Wright, A. D., Nelson, J. C. & Weichman, M. L. A versatile platform for gas-phase molecular polaritonics. *J. Chem. Phys.* **159**, 164202 (2023).
70. Wang, D. et al. Coherent coupling of a single molecule to a scanning fabry-perot microcavity. *Phys. Rev. X* **7**, 021014 (2017).
71. Chikkaraddy, R. et al. Single-molecule strong coupling at room temperature in plasmonic nanocavities. *Nature* **535**, 127–130 (2016).
72. Vahala, K. J. Optical microcavities. *Nature* **424**, 839–846 (2003).
73. Tanabe, T., Notomi, M., Kuramochi, E., Shinya, A. & Taniyama, H. Trapping and delaying photons for one nanosecond in an ultra-small high-q photonic-crystal nanocavity. *Nature Photonics* **1**, 49–52 (2007).
74. Takahashi, Y. et al. High-q nanocavity with a 2-ns photon lifetime. *Optics express* **15**, 17206–17213 (2007).

75. Nelsen, B., Liu, G., Steger, M. & Snoke, D. W. Dissipationless flow and sharp threshold of a polariton condensate with long lifetime. *Phys. Rev. X* **3**, 041015 (2013).
76. Abbarchi, M. et al. Macroscopic quantum self-trapping and josephson oscillations of exciton polaritons. *Nature Phys.* **9**, 275–279 (2013).
77. Dunkelberger, A., Spann, B., Fears, K., Simpkins, B. & Owrutsky, J. Modified relaxation dynamics and coherent energy exchange in coupled vibration-cavity polaritons. *Nature Commun.* **7**, 13504 (2016).
78. Minkov, M., Savona, V. & Gerace, D. Photonic crystal slab cavity simultaneously optimized for ultra-high q/v and vertical radiation coupling. *Appl. Phys. Lett.* **111**, 131104 (2017).
79. Pan, F. et al. Elucidating energy pathways through simultaneous measurement of absorption and transmission in a coupled plasmonic-photonic cavity. *Nano Lett.* **20**, 50–58 (2020).
80. Vuong, V. Q. et al. Parameterization and benchmark of long-range corrected dftb2 for organic molecules. *J. Chem. Theory Comput.* **14**, 115–125 (2018).
81. Porezag, D., Frauenheim, T., Köhler, T., Seifert, G. & Kaschner, R. Construction of tight-binding-like potentials on the basis of density-functional theory: Application to carbon. *Phys. Rev. B* **51**, 12947–12957 (1995).
82. Seifert, G., Porezag, D. & Frauenheim, T. Calculations of molecules, clusters, and solids with a simplified lcao-dft-lda scheme. *Int. J. Quant. Chem.* **58**, 185–192 (1996).
83. Elstner, M. et al. Self-consistent-charge density-functional tight-binding method for simulations of complex materials properties. *Phys. Rev. B* **58**, 7260–7268 (1998).
84. Hourahine, B. et al. Dftb+, a software package for efficient approximate density functional theory based atomistic simulations. *J. Chem. Phys.* **152**, 124101 (2020).
85. Kästner, J. et al. Dl-find: An open-source geometry optimizer for atomistic simulations. *J. Phys. Chem. A* **113**, 11856–11865 (2009).
86. Scully, M. O. & Zubairy, M. S. *Atom-field interaction - semiclassical theory*, 145–192 (Cambridge University Press, 1997).
87. Rabi, I. On the process of space quantization. *Phys. Rev.* **49**, 324–328 (1936).
88. Rabi, I. Space quantization in a gyrating magnetic field. *Phys. Rev.* **51**, 652–654 (1937).
89. Granucci, G., Persico, M. & Toniolo, A. Direct semiclassical simulation of photochemical processes with semiempirical wave functions. *J. Chem. Phys.* **114**, 10608–10615 (2001).
90. Tully, J. C. Molecular dynamics with electronic transitions. *J. Chem. Phys.* **93**, 1061–1071 (1990).
91. Ha, J.-K., Lee, I. S. & Min, S. K. Surface hopping dynamics beyond nonadiabatic couplings for quantum coherence. *J. Phys. Chem. Lett.* **9**, 1097–1104 (2018).
92. Han, D., Ha, J.-K. & Min, S. K. Real-space and real-time propagation for correlated electron-nuclear dynamics based on exact factorization. *J. Chem. Theory Comput.* **19**, 2186–2197 (2023).
93. Filatov, M., Min, S. K. & Kim, K. S. Direct nonadiabatic dynamics by mixed quantum-classical formalism connected with ensemble density functional theory method: Application to trans-penta-2,4-dieniminium cation. *J. Chem. Theory Comput.* **14**, 4499–4512 (2018).
94. Filatov, M., Paolino, M., Min, S. K. & Kim, K. S. Fulgides as light-driven molecular rotary motors: Computational design of a prototype compound. *J. Phys. Chem. Lett.* **9**, 4995–5001 (2018).
95. Filatov, M., Min, S. K. & Kim, K. S. Non-adiabatic dynamics of ring opening in cyclohexa-1,3-diene described by an ensemble density-functional theory method. *Mol. Phys.* **117**, 1128–1141 (2019).
96. Filatov, M., Min, S. K. & Choi, C. H. Theoretical modelling of the dynamics of primary photoprocess of cyclopropanone. *Phys. Chem. Chem. Phys.* **21**, 2489–2498 (2019).
97. Filatov, M., Paolino, M., Min, S. K. & Choi, C. H. Design and photoisomerization dynamics of a new family of synthetic 2-stroke light driven molecular rotary motors. *Chem. Commun.* **55**, 5247–5250 (2019).
98. Hellmann, H. *Einführung in die Quantenchemie*, 285. Franz Deuticke: Leipzig und Wien (1937).
99. Feynman, R. P. Forces in molecules. *Phys. Rev.* **56**, 340–343 (1939).
100. Pulay, P. Ab initio calculation of force constants and equilibrium geometries in polyatomic molecules. *Mol. Phys.* **17**, 197–204 (1969).
101. Lee, I. S. et al. Pyunixmd: A python-based excited state molecular dynamics package. *J. Comp. Chem.* **42**, 1755–1766 (2021).
102. Kim, T. I., Ha, J. K. & Min, S. K. Coupled- and Independent-Trajectory Approaches Based on the Exact Factorization Using the PyUNIxMD Package. *Top. Curr. Chem.* **380**, 1–27 (2022).
103. Jorgensen, W. L., Maxwell, D. S. & Tirado-Rives, J. Development and testing of the opls all-atom force field on conformational energetics and properties of organic liquids. *J. Am. Chem. Soc.* **118**, 11225–11236 (1996).
104. Rackers, J. A. et al. Tinker 8: Software tools for molecular design. *J. Chem. Theory Comput.* **14**, 5273–5289 (2018).

Acknowledgements

This research was supported by the National Research Foundation of Korea (NRF) funded by the Korean government (Ministry of Science and ICT (MSIT))(NRF-2023M3K5A1094813, RS-2023-00257666, RS-2024-00455131) and the IBS (IBS-R019-D1). Computational work for this research was partially performed on the Olaf supercomputer supported by the IBS Research Solution Center. ISL is grateful for the computational support from the Korea Institute of Science and Technology Information (KISTI) for the Nurion cluster (KSC-2024-CRE-0481).

Author contributions

I.S.L. developed the methodology and performed the molecular dynamics simulations. I.S.L., M.F., and S.K.M. analyzed the data and wrote the original draft. I.S.L., M.F., and S.K.M. edited and reviewed the manuscript. M.F. and S.K.M. supervised the work throughout.

Competing interests

The authors declare no competing interests.

Additional information

Supplementary information The online version contains supplementary material available at https://doi.org/10.1038/s41467-025-59607-3.

Correspondence and requests for materials should be addressed to Michael Filatov or Seung Kyu Min.

Peer review information *Nature Communications* thanks Stefano Crespi, Shaul Mukamel and the other, anonymous, reviewer(s) for their contribution to the peer review of this work. A peer review file is available.